Materials Today Bio 14 (2022) 100261

Contents lists available at ScienceDirect

Materials Today Bio

journal homepage: www.journals.elsevier.com/materials-today-bio

Hybridizing gellan/alginate and thixotropic magnesium phosphate-based hydrogel scaffolds for enhanced osteochondral repair

You Chen [a,b,1], Yuanyuan Chen [c,1], Xiong Xiong [c,1], Rongwei Cui [c], Guowei Zhang [c], Chen Wang [d], Dongqin Xiao [b,*], Shuxin Qu [a,**], Jie Weng [a]

[a] Key Laboratory of Advanced Technologies of Materials, Ministry of Education, School of Materials Science and Engineering, Southwest Jiaotong University, Chengdu, 610031, Sichuan, China
[b] Research Institute of Tissue Engineering and Stem Cells, Nanchong Central Hospital, The Second Clinical College of North Sichuan Medical College, Sichuan, China
[c] School of Life Science and Engineering, Southwest Jiaotong University, Chengdu, 610031, Sichuan, China
[d] School of Mechanical Engineering, Southwest Jiaotong University, Chengdu, 610031, Sichuan, China

ARTICLE INFO

Keywords:
Hybrid scaffolds
Osteochondral regeneration
Cartilage

ABSTRACT

Osteochondral defects include the damage of cartilage and subchondral bone, which are still clinical challenges. The general replacements are difficult to simultaneously repair cartilage and subchondral bone due to their various requirements. Moreover, appropriate printable bioactive materials were needed for 3D bioprinting personalized scaffolds for osteochondral repairing. Herein, the novel hydrogel was developed by hybridizing the alginate sodium (SA) and gellan gum (GG) with the inorganic thixotropic magnesium phosphate-based gel (TMP-BG) in the pre-crosslinking of Mg^{2+} to enhance osteochondral repairing. SA-GG/TMP-BG hybrid hydrogels possessed controllable rheological, injectable, mechanical properties and porosities by tuning their ratio. The shear-thinning of SA-GG/TMP-BG was responsible for its excellent injectability. SA-GG/TMP-BG hybrid hydrogels displayed good cell compatibility, on which MG-63 and BMSCs cells attached and spread well with the high proliferation and up-regulated osteogenic genes. In addition, the inorganic TMP-BG gel hybridized with SA-GG hydrogel released Mg^{2+} was conducive to recruiting BMSCs and promoting the osteogenic and chondrogenic differentiation of BMSCs. Histological results confirmed that SA-GG/TMP6040 significantly promoted the osteogenesis of subchondral bone and then further facilitated the cartilage repairing after being implanted in osteochondral defects of rabbits for 6 and 12 weeks.

Our finding revealed that the inorganic TMP-BG endowed the excellent osteogenic activity of the hybrid hydrogels, which played a key role in successful osteochondral repairing. The newly SA-GG/TMP-BG hybrid hydrogels appeared to be promising materials for osteochondral repairing and the further 3D bioprinting.

1. Introduction

Osteochondral lesions usually involve simultaneous injuries to the cartilage and subchondral bone, which seriously affect the life quality of patients [1]. Moreover, the ability of cartilage and subchondral bone to heal is also impaired by the injuries due to the lack of blood supply and metabolic activity [2,3]. Common clinical treatment strategies involve transplantation of autogenous bone [4], autologous chondrocytes [5], and micro-fracture surgery [6]. These options, however, are limited by the limited donor availability, immune rejection and unsatisfactory long-term outcomes [7]. Although hydrogel-based tissue engineering scaffolds are expected to be an effective method for osteochondral repair, simultaneous repair of cartilage and subchondral bone remains a challenge [8,9]. A common method is to prepare two materials and they are bonded for transplantation [10]. However, the poor interfacial bonding force easily leads to the separation of the two materials during implantation. Recently, 3D printing is emerging as a feasible technique to fabricate scaffolds with a gradient structure of osteochondral repair [11]. Nevertheless, there is a lack of appropriate printable bioactive materials.

* Corresponding author.
** Corresponding author.
E-mail addresses: xiaodongqin@nsmc.edu.cn (D. Xiao), qushuxin@swjtu.edu.cn (S. Qu).
[1] Y. Chen, YY Chen and X. Xiong contributed equally to this work.

https://doi.org/10.1016/j.mtbio.2022.100261
Received 30 January 2022; Received in revised form 26 March 2022; Accepted 10 April 2022
Available online 13 April 2022

In addition, minimally invasive surgery is the mainstream of joint repair. Therefore, it is urgent to develop materials with high injectability and bioactivity for both minimally invasive surgery and 3D printing.

Hydrogels are widely used as bioactive biomaterials due to their excellent biocompatibility, 3D network structure similar to extracellular matrix, good permeability and controllable mechanical properties [12,13]. Natural hydrogels provide more adhesion sites for cells and subsequently promote their functional expression and reduce immune rejection *in vivo*, but are frequently unsatisfactory in mechanical strength [14].

Hence, composites with tunable properties are expected to solve the above problems. In particular, inorganic phase plays important roles in the bone. Du et al. constructed a hydroxyapatite (HA)/PCL composite scaffold with gradient mechanical properties and ingredients *via* 3D printing to promote osteochondral repair [15]. In addition, the mechanical strength of the composite scaffolds could be accurately controlled by adjusting the ratio of inorganic bioactive components of polymer materials [16]. However, it is still difficult to satisfy the multiple demands of osteochondral repair due to the complicated preparation process, limited bioactivity, and high cost. Preparation of hybrid tissue engineering materials by combing bioactive ingredients and hydrogels is expected to improve the osteochondral repaired ability of materials [17]. However, when the size of cartilage lesions are large accompanying with the subchondral bone, it is still a severe challenge [18]. In addition, studies reported that the core problem of osteochondral repair is fast regeneration of the subchondral bone, which provides a good mechanical support for subsequent repair of the cartilage [19]. Therefore, how to improve the priority repairing of subchondral bone is one of the challenges for osteochondral regeneration.

Magnesium is the fourth largest metal element in the human body. About 60% of the magnesium is found in the bone matrix, promoting the adhesion, proliferation and differentiation of cells, inducing the deposition of bone minerals, and facilitating osteogenesis [20,21]. Magnesium phosphate bone cement and magnesium metal have been extensively used for orthopaedics [22,23]. However, magnesium phosphate bone cement generally has complicated components accompanied by a relatively intense heat release during setting [24]. The *in vivo* degradation rate of magnesium metal is too fast, resulting in a local alkaline environment and gas accumulation [25]. Nano-magnesium phosphate material has good biological activity, which can promote bone tissue regeneration, thereby advancing the potential application for cartilage healing [20]. Our previous study prepared a thixotropic nano-magnesium phosphate-based gel material (TMP-BG) mainly composed of $MgNa_3H(PO_4)_2$, which combined bioactivity, injectability and formability due to its formulation and thixotropic properties [26]. Moreover, sodium alginate (SA) and gellan gum (GG) were added into TMP-BG to prepare a homogeneous SA-GG/TMP-BG hybrid bioink by pre-crosslinking of Mg^{2+} for 3D bioprinting [27]. Interestingly, mechanical properties of SA-GG/TMP-BG hybrid bioinks depended strongly on their composition. This hybrid bioinks were expected to be printed into cell-loaded scaffolds *via* 3D bioprinting for tissue repair. However, the application of the SA-GG/TMP-BG hybrid material for osteochondral repair has not been studied.

In this study, the effects of TMP-BG on the physicochemical properties of SA-GG/TMP-BG scaffolds were examined. The biocompatibility and bioactivity of SA-GG/TMP-BG were investigated *via* cell culture and *in vivo* rabbit cartilage defect model implantation. The mechanism of osteochondral repair regulation by this new SA-GG/TMP-BG hybrid material was revealed.

2. Materials and methods

2.1. Synthesis of hybrid hydrogel scaffolds

Inorganic TMP-BG were prepared as described previously [26]. Briefly, the molar ratios of $NaOH/H_3PO_4/Mg(OH)_2$ were chosen to be 2.87/2/1 to give a stable inorganic gel. Secondly, the 2.5% sodium alginate (SA, 180,947, Sigma) −3.0% gellan gum (GG, G3251, Phyto-Tech) with good gelation properties and mechanical strength was selected as the organic component [27]. The SA-GG and TMP-BG were mixed thoroughly to prepare SA-GG/TMP-BG hybrid hydrogel. Finally, hybrid hydrogel scaffolds were produced by crosslinking with 0.5 M $CaCl_2$ for 24 h. Four formulations of SA-GG/TMP-BG hydrogels are studied (Table 1).

Table 1
Proportion of hybrid organic/inorganic sodium alginate-gellan gum/magnesium phosphate-based.

Samples	SA-GG (v/v %)	TMP-BG (v/v %)
SA-GG	100	0
SA-GG/TMP8020	80	20
SA-GG/TMP6040	60	40
SA-GG/TMP4060	40	60

2.2. Physicochemical characterization

2.2.1. Rheology

The rheological behavior of four hybrid pre-gel (paste) was measured on a Rotational Rheometer (DHR-1, TA, USA) with a parallel plate configuration (diameter 20 mm, gap 1 mm) by three procedures. First, the linear viscoelastic region (LVR) of four samples was measured by the amplitude (strain) sweep, with the oscillating strain increase from 0.001% to 50% at a constant frequency of 1 Hz. Second, the dynamic viscosity of four samples was evaluated by the shear rate increasing from 0.001 to 50 s^{-1}. Finally, the frequency range of 0.1–100 Hz was performed at the fixed shear strain within the LVR to measure the dynamic storage modulus (G′) and loss modulus (G″). Each test procedure requires 500 μL of samples to be added to the plate.

2.2.2. Compressive test

Compressive testing of different hydrogel discs (Φ 20 × 8 mm) was determined by using a Universal Mechanical Machine (5567, Instron, USA) on the compression rate of 0.5 mm/min until a 70% compressive strain. The compressive stiffness was calculated on the basis of the linear deformation region of the stress-strain curve from 5% to 15% of compressive strain [28]. The maximum compressive stress was identified as the stress, by which all the hydrogel discs were subjected to being destroyed.

2.2.3. FTIR and TGA

Fourier Transform Infrared Spectroscopy (FTIR, 5700, Nicolet, USA) was utilized to investigate whether there was an interaction of functional groups among TMP-BG and SA/GG. All the hydrogels were dried, powdered, mixed with KBr and then pressed into disks prior to characterization. Thermal Gravimetric tests were performed using a thermal analyzer (TG209F1, Netzsch, German) where the sample was heated at a rate of 10 °C/min under a dynamic N_2 flow with a temperature range from room temperature to 800 °C.

2.2.4. Microstructure

The morphology of four hydrogels was characterized by scanning electronic microscopy (SEM, QUANTA FEG 250, FEI, USA). Samples were freeze-dried by Lyophilizer (FreeZone, Labconco, USA) for 3 d. Then, the porosity of these samples was determined using the software Image-J.

2.2.5. Biomineralization

The crosslinked hydrogels were cut into discs (Φ20 × 8 mm) and then suspended in 40 mL of simulated body fluids (SBF) at 37 °C for 15 d. The SBF was changed once a week and prepared according to a previous study [29]. After 15 d, the samples were taken out and rinsed twice with deionized water, and then freeze-dried for 3 d. The surface morphology and composition was measured by SEM and X-Ray Diffraction (XRD,

Philips, Netherlands).

2.3. In vitro cytocompatibility

2.3.1. Cell culture

The human osteoblastic cell MG-63 was cultured in DMEM (Gibico, USA) with a 10% fetal bovine serum (FBS, ExCell, China), 1% penicillin and streptomycin (Sigma-Aldrich, USA), which were kindly provided by Sichuan University (Chengdu, China). Four hydrogel discs (Φ20 × 8 mm) sterilized by pasteurization were placed in 6-well plates, seeded with MG-63 cells (5×10^4 cells/sample) and incubated for 1–7 d. Culture medium was exchanged every two days. The only MG-63 cells without the samples were treated as the control group. Each group was in triplicate.

2.3.2. Cell staining and analysis of proliferation

The MG-63 cells were stained with Rhodamine 123 (Rh123, R8004, Sigma-Aldrich, USA) and 4′, 6-diamidino-2-phenylindole (DAPI, 4A Biotech, China). In detail, 3 mL of 10 μg/mL Rhodamine 123 was added to 6-well plates and incubated at 37 °C for 30 min. Subsequently, 1 mL of 1 μg/mL DAPI solution was poured into each well for 5 min of culture. Cells were viewed under a fluorescence microscope (MXH-100, Motic, China).

Proliferation of MG-63 cells was measured by Alamar blue (AB, Invitrogen, USA) assay. After culture for 1, 3, 5 and 7 d, the cell culture medium was replaced with the fresh cell culture medium containing 10% Alamar Blue reagent. The 6-well plates were then cultivated for 4 h. Subsequently, 100 μL of incubated medium were aspirated and measured with a microplate reader (μQuant, Bio-Tek, USA) at 570 and 600 nm, respectively [30].

2.3.3. Real-time qPCR assay for bone-specific genes

At the scheduled incubation time, the MG-63 cells were digested with Trypsin (Sigma-Aldrich, USA) and collected. Total RNA was collected using Trizol reagent (Ambion, USA) following the manufacturer's protocol. The cDNA was synthesized using a cDNA reverse transcription kit (Thermo, USA) with the manufacturer's instruction. The resulting cDNAs were conducted by using SYBR Green detection reagent (DBI-2220 Bestar, German) on a real-time quantitative PCR (Bio-Rad, CFX96, USA). Relative expression was evaluated using the $2^{-\Delta\Delta Ct}$ method and the housekeeping gene GAPDH was employed as a reference gene. To calculate the relative value of gene expression, the MG-63 cell culture plate served as a control and was set as 1. Primers used to amplify bone-specific genes are shown in Table.S1.

2.4. Regulation of materials on biological functions of BMSCs

2.4.1. Scratch test and transwell assay

Bone marrow-derived mesenchymal stem cells (BMSCs) were isolated bilaterally from the femurs of 3 week-old male SD rats [31]. The BMSCs (1×10^5) were seeded in a 12-well plate and cultured for 24 h. The cell surface was with scratched a sterile 200 μL pipette tip. Then, the cells were cultured with the samples of PBS (control group), SA-GG, SA-GG/TMP6040 hydrogels in the F12 DMEM medium. Light photomicrographs were taken at 0 and 24 h.

Transwell assays were performed using Transwell chambers (Corning, New York, USA). BMSCs (5×10^4) were seeded in the upper chamber containing serum-free medium and then the samples of PBS, SA-GG, SA-GG/TMP6040 hydrogels were added. Then the Transwell was placed into a 24 well-plate with serum-containing medium. After culture for 24 h, the BMSCs in the upper chamber were removed. The cells migrating to the lower layer were stained by immersing the Transwell in 0.1% crystal violet solution for 30 min (Solarbio, China), and then observed under a light microscope.

2.4.2. Proliferation and cell morphology of BMSCs cultured with hydrogels

BMSCs (5×10^4, passage 3) were seeded on the surface of petri dish, SA-GG, SA-GG/TMP6040 hydrogels. The proliferation and cell morphology of BMSCs were measured by the Live/Dead cell staining kit (Meilunbio, China) and Alexa Fluor 594 labeled phalloidin cell staining (Biotech, China) after 3 d of incubation with hydrogels. Cells were observed under a fluorescence microscope (MXH-100, Motic, China).

2.4.3. Effects of hydrogels on differentiation of BMSCs

The BMSCs (2×10^4, passage 3) were plated into 12-well plates and cultured in F12 DMEM medium for 12 h, after which the culture medium was changed to osteo-inductive medium (complete medium supplemented with 10 mM β-glycerophosphate, 10 nM dexamethasone, and 50 μM vitamin c). The hydrogels were added and cultured with BMSCs for 7 d. The medium was changed 3 times per week. To evaluate the ability osteogenic differentiation of BMSCs, the alkaline phosphatase (ALP) and mineralization nodule were measured by using ALP kit (Beyotime institute of Biotechnology, China) and alizarin red S (Solarbio, China) staining after then the BMSCs were fixed with 4% paraformaldehyde. For cartilage differentiation, the medium was changed to chondrogenic medium (10 ng/mL transforming growth factor-β3, 100 nM dexamethasone, 50 μM ascorbic acid 2-phosphate and 20 μM L-proline). The subsequent treatment of BMSCs in the 7 d culture was consistent with osteogenesis induction, and then the BMSCs were fixed and stained with Alcian blue staining solution (Solarbio, China). Also, the immunofluorescence staining of collagen II (CoL II) was used to analyze chondrogenic differentiation. All the images were captured with a fluorescence microscopy (LSCM, A1, Nikon, Japan).

2.5. In vivo animal experiments

2.5.1. Hybrid hydrogel scaffolds implantation

All the animal experiments were approved by the Animal Ethics Committee of Southwest Jiaotong University. As illustrated in Fig. 1, the SA-GG was hybridized with TMP-BG and then was crosslinked with $CaCl_2$ to form SA-GG/TMP-BG hybrid hydrogel scaffold. After cutting into discs, the hybrid hydrogel scaffolds were implanted into the knee defects. Briefly, a total of 18 New Zealand white rabbits (male, 2.5 ± 0.2 kg) were used for the *in vivo* test. The rabbits were randomly divided into three groups: the control group (non-implantation) and two experimental groups (SA-GG and SA-GG/TMP6040). After anesthetization with sodium pentobarbital solution (3% w/v, 1 mL/kg)) through the ear vein, a hole was drilled on the patellar groove of the right femur through the articular cartilage and subchondral bone to create a full-thickness defect (Φ 3.5 mm, height: 3 mm) [32]. The hydrogels (Φ 3.5 × 3 mm) were transplanted into the osteochondral defects. The inflammation of rabbits were detected and monitored by blood sample analysis 3 d after implantation. Briefly, the blood cell (WBC), granulocyte, lymphocyte, and intermediate cell, were analyzed with a XT-1800i automated hematology system (Sysmex, Shanghai, China). The ratio of inflammatory cells to WBC was calculated. After 6 and 12 weeks of implantation, the rabbits were killed by injection of sodium pentobarbital, and the knee joints containing hydrogels were harvested.

2.5.2. Gross observation

The harvested knee joints were pictured with a digital camera to evaluate tissue repair. Tissue regeneration was preliminarily determined according to the International Cartilage Repair Society (ICRS) histological grading system [33,34].

2.5.3. Histological analysis

The harvested samples were rinsed with PBS, fixed in 10% neutral-buffered formalin for 7 d, decalcified with 10% EDTA solution for 1 month, dehydrated with gradient ethanol solutions, cleared with xylene and embedded in paraffin. The samples were cut into 2 μm sections perpendicular to the bone. After then, the sections were stained with hematoxylin and eosin (H&E), safranin-O (Saf-O) and Collagen II (CoL II) to evaluate cartilage and subchondral bone regeneration and maturity of

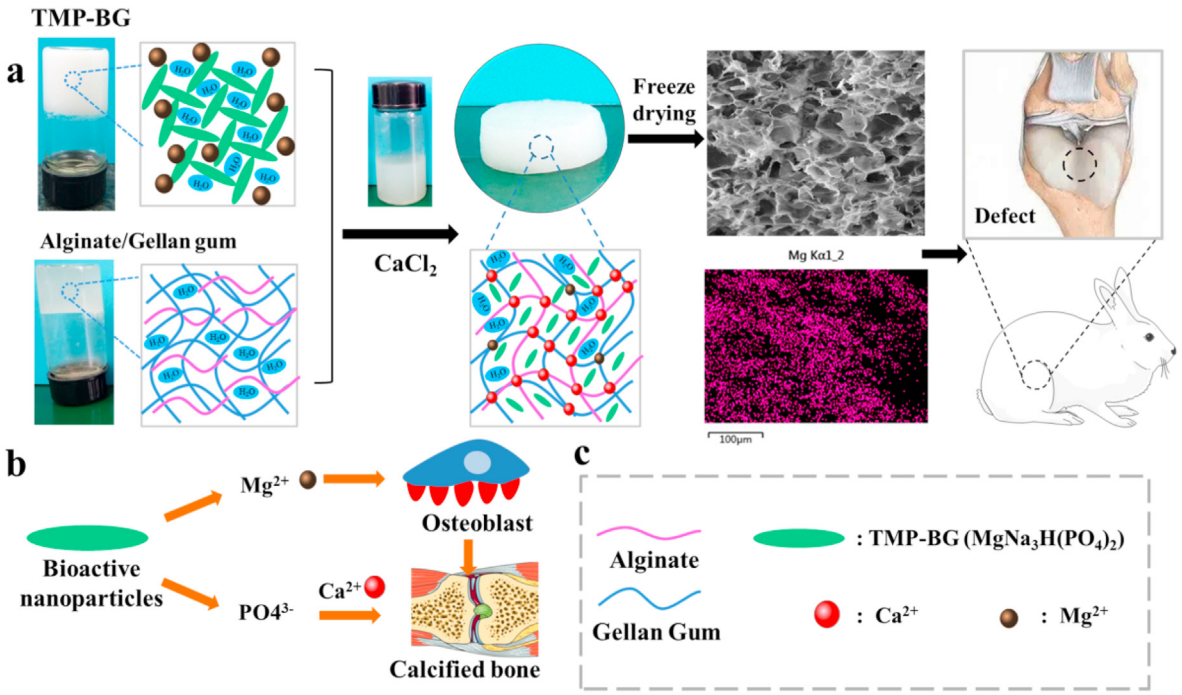

Fig. 1. (a) Schematic of the preparation of SA-GG/TMP-BG hybrid hydrogel scaffolds and its implantation of osteochondral injury of rabbit knee joint. The EDS element distribution of Mg indicates uniform distribution of inorganic TMP-BG. (b) The mechanism of TMP-BG promoting bone regeneration and (c) description of legend.

the newly regenerated tissue. The histological assessment of the cartilage effect of tissue regeneration was determined according to the ICRS histological grading system [35]. The rate of subchondral bone regeneration was confirmed with the Image-J software. Briefly, the calculation of the subchondral bone area ratio was based on the percentage of the area of bone matrix in the × 4 images.

2.5.4. Fluorescent bone labeling

Three fluorescent bone markers, calcein, tetracycline and alizarin, were used to determine the new bone formation during tissue regeneration. These markers were injected into rabbits through the ear vein at 6, 8 and 10 weeks of implantation (Table.S2). Briefly, three different concentrations of fluorescent bone markers were dissolved 2% $NaHCO_3$ saline and then injected into rabbits at different schedules. The knee joints were harvested after 12 weeks of implantation. Then these samples were fixed, dehydrated and embedded in poly (methylmethacrylate). The embedded specimens were cut into 100 μm sections perpendicular to the bone and then grounded and polished to a final thickness of ~50 μm for imaging with a laser scanning confocal microscope (LSCM, A1, Nikon, Japan). Fluorescent labeling with new bone formation was quantified using Image-J software (National Institutes of Health, latest version).

2.6. Statistical analysis

Data were analyzed by one-way analysis of variance (ANOVA) followed by Tukey test. A value of $p < 0.05$ was considered statistically significant.

3. Results and discussion

3.1. Synthesis and characterization of hybrid SA-GG/TMP-BG pre-gels

Fig. 2a shows the appearance of four SA-GG/TMP-BG hybrid hydrogels with different ratios. They did not flow when positioned upside down, and the transparency of the hybrid hydrogels gradually decreased with the increase of TMP-BG. It suggested that four hybrid hydrogels with different ratios appeared in a gel-like state, which was caused by the crosslinking of GG by the magnesium ions of TMP-BG to forming a weak gel [27]. The pH of SA-GG, SA-GG/TMP8020, SA-GG/TMP6040 and SA-GG/TMP4060 were 6.63 ± 0.12, 7.13 ± 0.11, 7.33 ± 0.12 and 7.50 ± 0.10, respectively (Fig. 2b). Compared with SA-GG group, the pH of hybrid hydrogel slightly increased, which may be attributed to the increase of alkaline TMP-BG content (7.65 ± 0.01) [26]. The pH value of all hybrid scaffolds are within the safe range of cell compatibility, so there will be no cell damage.

Fig. 2c shows the results of the rheological properties of four hybrid hydrogels. Amplitude sweeps found that the storage modulus (G′) and loss modulus (G″) of four hybrid hydrogels passed through a plateau with increasing oscillation strain, and then slowly decreased until the intersection of G′ and G". The front plateau area was the linear viscoelastic area (LVR) of the hybrid hydrogels [26]. Rheological properties are related to the structural stability, fluidity and dispersion stability of material [36]. Present rheological properties indicated that the structure of the hybrid hydrogels was not destroyed within the LVR whereas exhibited a flow state when the G′ and G″ intersected [37]. Fig. 2c shows that the LVR of SA-GG was the largest (black dotted line), and the strain was ≤ 0.8%, while the LVR of SA-GG/TMP-BG8020, SA-GG/TMP6040 and SA-GG/TMP4060 was ≤ 0.008% (blue dotted line), 0.02% (pink dotted line) and 0.1% (red dotted line), respectively. It indicated that the addition of inorganic TMP-BG hydrogel reduced the structural stability of the hybrid SA-GG/TMP-BG. Fig. 2d shows the shear thinning behavior of different four SA-GG/TMP-BG hybrid hydrogels with different ratios, which was accelerated by the increase of TMP-BG owing to the thixotropy of TMP-BG (Fig. S1a-c). TMP-BG formed a “house of cards” reversible structure (Fig. S1d) revealed by SEM through electrostatic attraction between particles (Fig. S1e), which resulted in the thixotropy of TMP-BG [26]. The G′ and G″ of SA-GG/TMP-BG hybrid hydrogels did not change significantly with the increase of shear frequency (Fig. 2e), which indicated a good dispersion of hybrid hydrogels [26]. In addition, the value of Tan δ = G′/G″ was less than 1 during the change of shear frequency (Fig. 2f), which further confirmed that all four samples exhibited a gel-like state [38]. Gel-like and well-dispersed hybrid

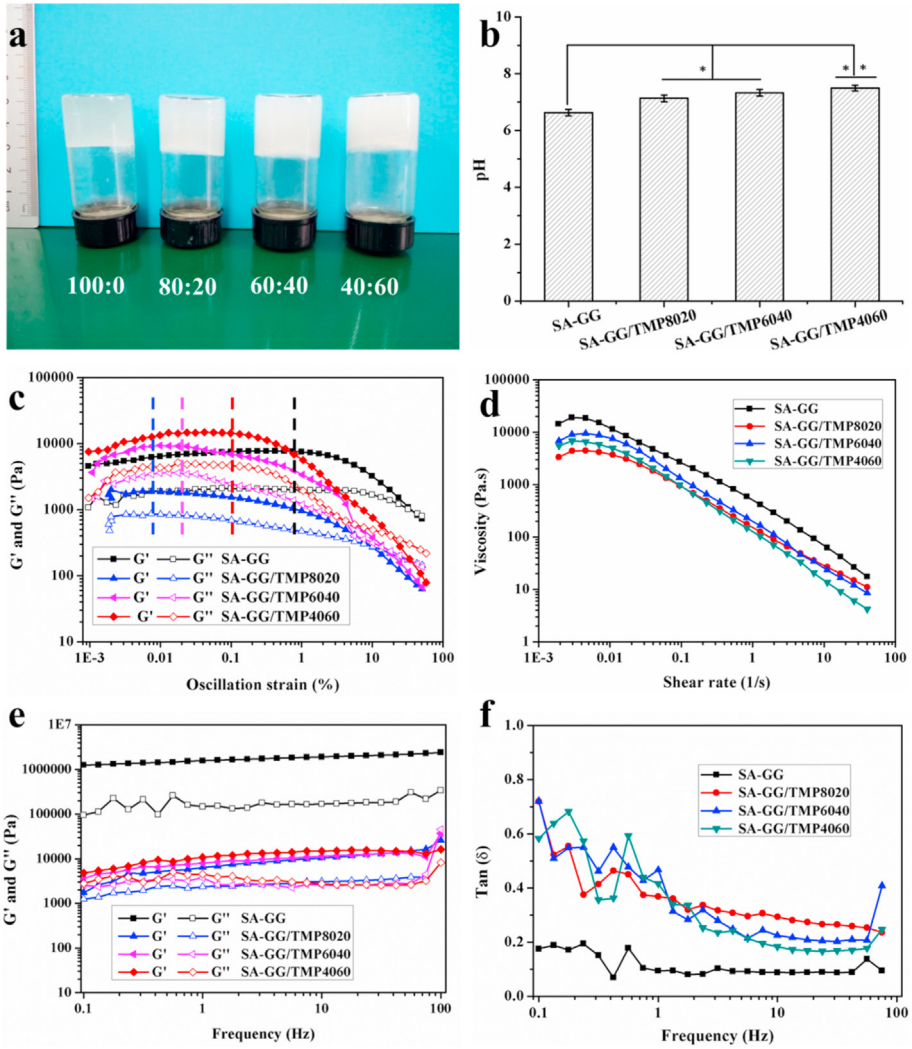

Fig. 2. (a) The optical images of SA-GG/TMP-BG with different ratios (SA-GG: TMP-BG) and (b) their pH values. Rheological results of four different proportions of SA-GG/TMP-BG hybrid pre-gel: (c) Amplitude scanning results, strain range from 0.001% to 50%; (d) Viscosity versus shear rate curves; (e) Results of frequency scanning and (f) Results of tan δ result graph. $^{*}p < 0.05$, $^{**}p < 0.01$; n = 3.

hydrogels would be better used as injectable and printable biomaterials. The preliminary results of 3D bioprinting experiments are shown in Fig. S2. In addition, not only the complex three-dimensional structures could be printed (Fig. S2a-d), but also loaded cells in hybrid bioinks could be printed. After printing, the cells possessed a good survival rate (Fig. S2e, f), which was reported in detail in our previous work [27]. These results indicated that the hybrid hydrogels were expected to construct a cell-loaded tissue engineering scaffold for *in vivo* tissue repairing or organoid model for drug screening or disease studying in the future.

3.2. Characterization of hybrid hydrogel scaffolds

The crosslinked hybrid hydrogels appeared as gel discs (Fig. 3a), which appeared smooth and translucent. With increasing TMP-BG, the hybrid hydrogel scaffolds changed from opaque to white with a rough surface, which may facilitate cell adhesion and tissue integration. The compressive stiffness of the SA-GG hydrogel scaffold reached 400 kPa (Fig. 3b), which was higher than some natural hydrogels [e.g., gelatin acrylate (35 kPa), polyvinyl alcohol acrylate (20 kPa), agarose 18 (kPa), alginate (5 kPa)] [39]. When the content of TMP-BG in the SA-GG was increased to 20%, 40%, and 60% (all v/v), the compressive stiffness of the scaffolds decreased to 200 kPa, 125 kPa, and 110 kPa, respectively, which are higher than some hydrogel scaffolds used in tissue engineering [40,41]. The results indicated that the mechanical properties of the hybrid hydrogel scaffolds could be tuned by adjusting the SA-GG/TMP-BG ratio.

As is well known, the mechanical strength of scaffolds is a key factor affecting bone regeneration. Reasonable control of the mechanical strength of the scaffolds is beneficial to reduce the interfacial stress between the material and the defects, and to accurately control the differentiation potential of mesenchymal stem cells into bone or cartilage [42]. The compressive stiffness of the knee joint hyaline cartilage, fibrocartilage and cartilage in the depth zone was 0.2–2 MPa [43], 0.1–0.3 MPa [44,45], and 10 MPa [43], respectively. The present hybrid scaffolds were suitable for fibrous cartilage and hyaline cartilage, but there was still a challenge to the application of high-strength cartilage and load-bearing bone. It is expected that the mechanical strength of these hybrid scaffolds will be further improved by changing the concentration of SA-GG and the cross-linking method in the future. The stress-strain curves in Fig. 3c show that the ultimate strain of the SA-GG was 55% when it reached 70% for the SA-GG/TMP8020, which suggested the

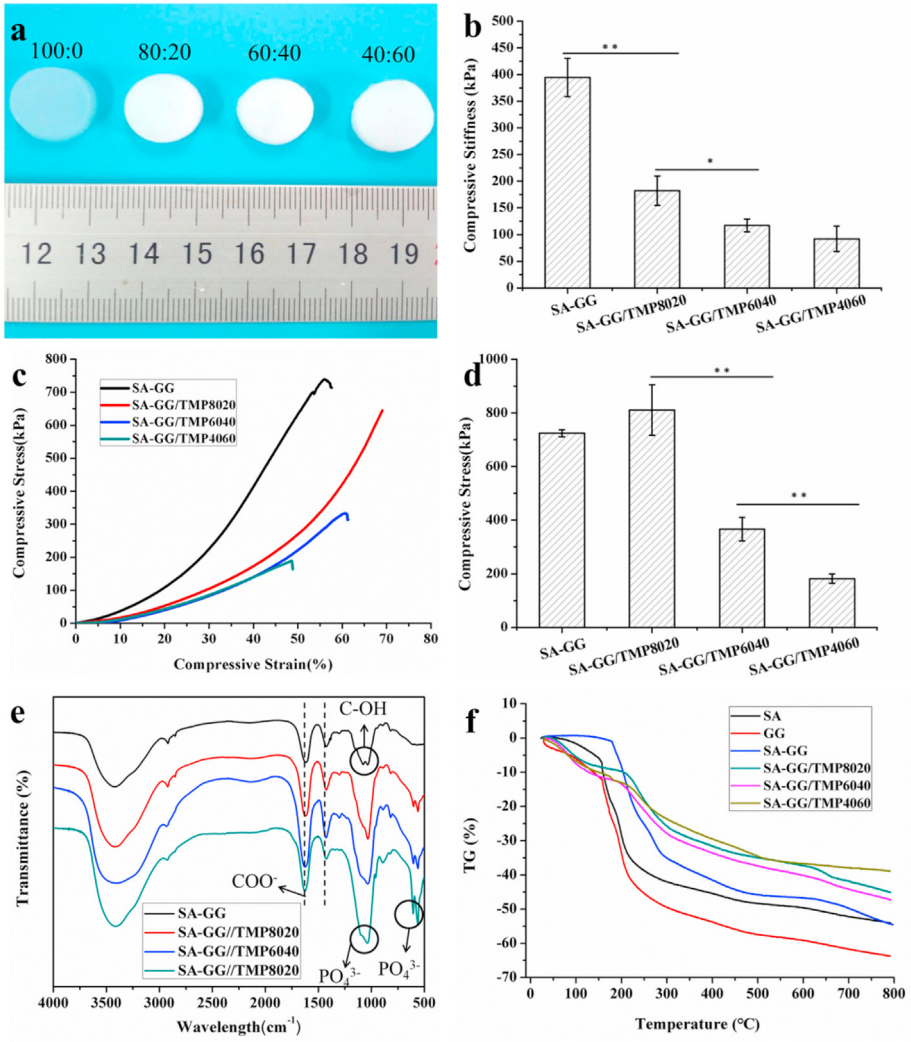

Fig. 3. (a) The formed of SA-GG/TMP-BG hybrid hydrogels indicated in the upper of images; (b) Results of compression modulus; (c) Typical stress-strain curves; (d) The maximum compressive stress when the sample was compressed to failure. (e) FTIR results of SA-GG/TMP-BG hybrid samples; (f) Thermogravimetric curves of SA , GG and SA-GG/TMP-BG hybrid scaffolds. $*p < 0.05$, $**p < 0.01$; n = 3.

addition of TMP-BG improved the toughness of the hybrid hydrogel scaffold. However, it would decrease the toughness of the hybrid hydrogel scaffold when the added TMP-BG was excessive. For example, the ultimate strains of SA-GG/TMP6040 and SA-GG/TMP4060 were reduced to 60% and 48%, respectively. Fig. 3d shows the maximum load stress of the hybrid hydrogel scaffolds before structural failure during compression testing. The SA-GG/TMP8020 hydrogel scaffold could withstand the load stress of 811 ± 94 kPa and then decreased with the increase of TMP-BG (367 ± 43 kPa for SA-GG/TMP6040 and 181 ± 17 kPa for SA-GG/TMP4060), which was similar to the trend of compressive stiffness.

On FTIR spectra, a strong stretching vibration absorption attributed to C–OH groups of SA-GG appeared at about 1034 cm^{-1} and 1078 cm^{-1} (Fig. 3e), and the presence of COO^- of SA-GG was confirmed according to the vibrational modes at the band at 1424 cm^{-1} and 1617 cm^{-1} in SA-GG [46]. There was no significant change in the spectrum of the hybrid hydrogel scaffold when it was incorporated with TMP-BG. Compared with the SA-GG, two new peaks appeared at 561-605 cm^{-1}, which were assigned to the symmetrical bending vibration absorption peak of PO_4^{3-} in TMP-BG [47]. In addition, the absorption peak of C–OH with SA-GG around 1000 cm^{-1} was smooth and wide owing to the addition of TMP-BG, which was due to the superposition of the symmetric stretching vibration of PO_4^{3-} peaked at 1037 cm^{-1} and the absorption peak of C–OH group. The positions of characteristic absorption peaks for COO^- and PO_4^{3-} in SA-GG and TMP-BG did not shift significantly, which indicated no obvious interaction between SA-GG and TMP-BG [48]. Fig. 3f represents the thermogravimetric (TG) diagram of SA, GG and SA-GG/TMP-BG hybrid hydrogel scaffolds with different ratios. The TG curve for GG shows the fastest weight loss rate at around 30–200 °C, followed by SA, and finally SA-GG, which was attributed to water loss. In addition, thermal decomposition temperatures of GG and SA were about 249 °C [49] and 237 °C [50], respectively. Therefore, the weight loss of the SA, GG and SA-GG was enhanced when above 200 °C owing to polymer chains breaking and gradually decomposing. In addition, the weight loss of SA, GG and SA-GG were about 50%, 65% and 50% under the temperature of 800 °C, respectively. After adding TMP-BG, the loss weight rate of SA-GG became slow before 250 °C, mainly including the decomposition of water and part of SA and GG. In addition, the weight loss rate of the ternary hybrid hydrogel of SA-GG/TMP-BG was slower than that of SA, GG and SA-GG during the process of heating to 800 °C, and the weight loss rate of SA-GG/TMP4060 was the slowest. The weight loss of SA-GG/TMP8020, SA-GG/TMP6040 and SA-GG/TMP4060 at 800 °C was 44%, 46% and 38%, respectively. It might be that the hybrid hydrogel scaffolds had more crystallization zone and interpenetrating network structures, which resulted in reducing the thermal decomposition rate and improved thermal stability of the hybrid hydrogel scaffolds [49].

3.3. Microstructure of hybrid hydrogel scaffolds

Fig. 4 shows the morphology of the hybrid hydrogel scaffolds. As shown in Fig. 4b, the SA-GG exhibited a non-uniform porous structure with pore sizes ranging from 100 to 210 μm. The pore size of hybrid scaffolds gradually decreased with the increase of TMP-BG, which were ~40, 25 and 10 μm for SA-GG/TMP8020 (Fig. 4b), SA-GG/TMP6040 (Fig. 4c) and for SA-GG/TMP4060 (Fig. 4d), respectively. In addition, the porosity of SA-GG, SA-GG/TMP8020, SA-GG/TMP6040, and SA-GG/TMP4060 were about 80%, 70%, 57%, and 48%, respectively (Fig. 4e). Inorganic particles filled partially the network of hydrogel, which resulted in a decrease of porosity [41,51]. Therefore, we speculated that TMP-BG nanoparticles (Fig. S1f, g) could easily fill the macropore of SA-GG hydrogel, thus reducing the porosity and pore size of SA-GG hydrogel. A porous structure of biomaterials or tissue engineering scaffold could be beneficial to the ingrowth of tissue and cell [52]. It was reported that the scaffolds with 5–15 μm pores were conducive to the growth of fibroblasts, 20–125 μm were conducive to the penetration of mammalian cells, and 40–100 μm was promoted to the growth of osteoid [53]. Therefore, it is important to adjust the porosity and pore size of the scaffolds. Fig. 4f shows that the colors of the four hybrid scaffolds gradually fade with the increase of TMP-BG, which indicated the ability of samples of absorbing medium was reduced. In addition, the swelling rate of the hybrid scaffolds further confirmed the above results (Fig. S3). Therefore, the porosity and pore size of SA-GG could be adjusted by changing the ratio of TMP-BG, which was better for a scaffold with bone repair performance.

3.4. Biomineralization

Fig. 5 shows the morphology and phase component of the hybrid scaffolds after soaking in SBF for 15 d. The products were generated on the surface of the SA-GG scaffold (Fig. 5a), while the clustered, flaky and dense rod-like bone-like apatite appeared on the surface of SA-GG/TMP8020 (Fig. 5b), SA-GG/TMP6040 (Fig. 5c) and SA-GG/TMP4060 (Fig. 5d), respectively. The higher the TMP-BG content, the more osteoid apatite was acquired. This indicated that the different contents of TMP-BG in hybrid scaffolds could promote the formation of bone-like apatite with various amounts and shapes. XRD results showed that the diffraction peaks of the surface substances of the four samples matched well the diffraction peaks of hydroxyapatite (HA, JCPDS 09–0432) (Fig. 5e). Three maximum diffraction peaks of (211), (002), and (222) of HA appeared no shift in position, which suggested that the hybrid scaffolds enhanced the formation of HA. Studies reported that the scaffold enhanced its *in vitro* mineralization in SBF, confirming it's good osteogenic activity [29]. Therefore, the addition of TMP-BG enhanced the osteogenic activity of the hybrid hydrogel scaffolds.

3.5. In vitro cytotoxicity

Fig. 6a shows the results of cell staining after the co-culture of MG-63 cells and scaffolds for 1 d and 3 d. On day 1, the MG-63 cells were spindle-shaped with protruded pseudopodia as the normal morphology of MG-63 cells. After 3 d of co-culture, the number of MG-63 cells increased significantly, which showed normal morphology with a spread and large nucleus (blue) and the visible cytoplasm (green) was visible. It was consistent with our previous results, that the TMP-BG was conducive to promoting cell adhesion and proliferation [26,27]. Previous reports also showed that magnesium phosphate-based materials could promote the adhesion and proliferation of cells [20]. The quantitative results calculated by Image-J software showed that the cells increased significantly after 3 d of co-culture as shown in Fig. 6b. The proliferation rate of MG-63 cells gradually increased at 1 d, 3 d, and 5 d, and a slight decline was observed at 7 d due to the large number of cells resulting in insufficient space for cell growth (Fig. 6c). After co-culture for 5 d, the cellular proliferation rate on SA-GG, SA-GG/TMP8020, SA-GG/TMP6040 and SA-GG/TMP4060 were 141%, 143%, 160%, and 152%, respectively. Therein, SA-GG/TMP6040 had the largest cell proliferation rate at different time and possessed the best cell compatibility. In addition, it was shown that the cell proliferation rate increased with the TMP-BG increasing among the groups of SA-GG, SA-GG/TMP8020, and SA-GG/TMP6040. However, the proliferation rate slightly decreased

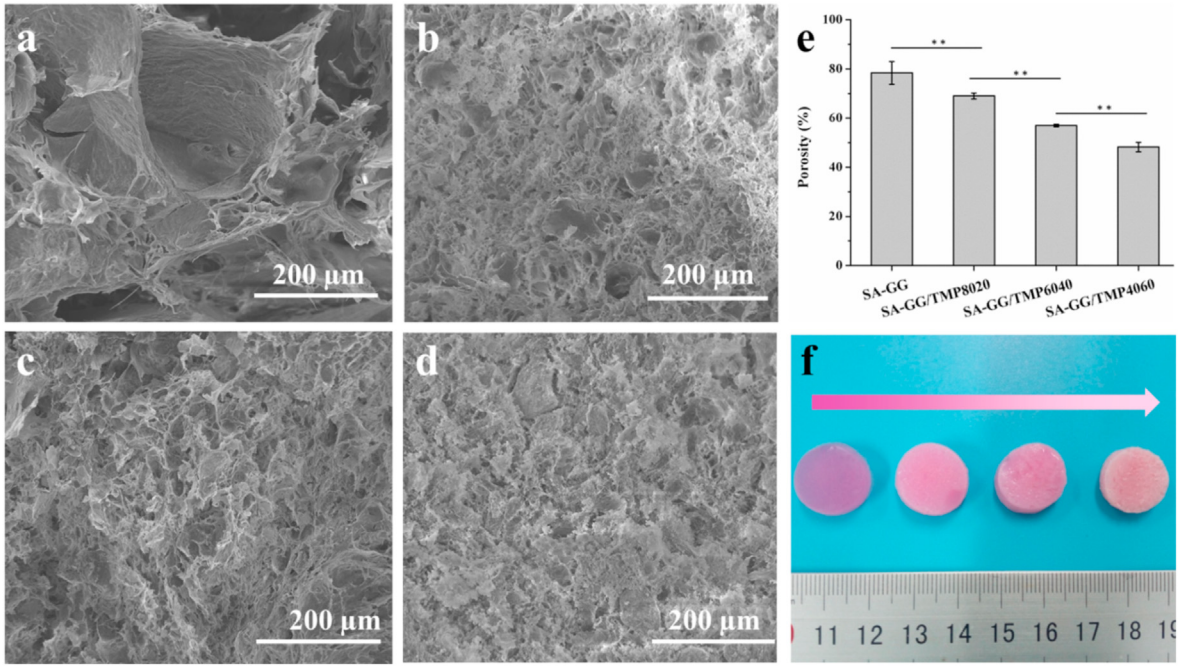

Fig. 4. SEM images of cross-section of hybrid hydrogel scaffolds (a) SA-GG, (b) SA-GG/TMP8020, (c) SA-GG/TMP6040, (d) SA-GG/TMP4060 and (e) The quantitative porosities. (f) Optical images of the hybrid hydrogel scaffolds after soaking in culture medium for 1d. $^{*}p < 0.05$, $^{**}p < 0.01$; n = 3.

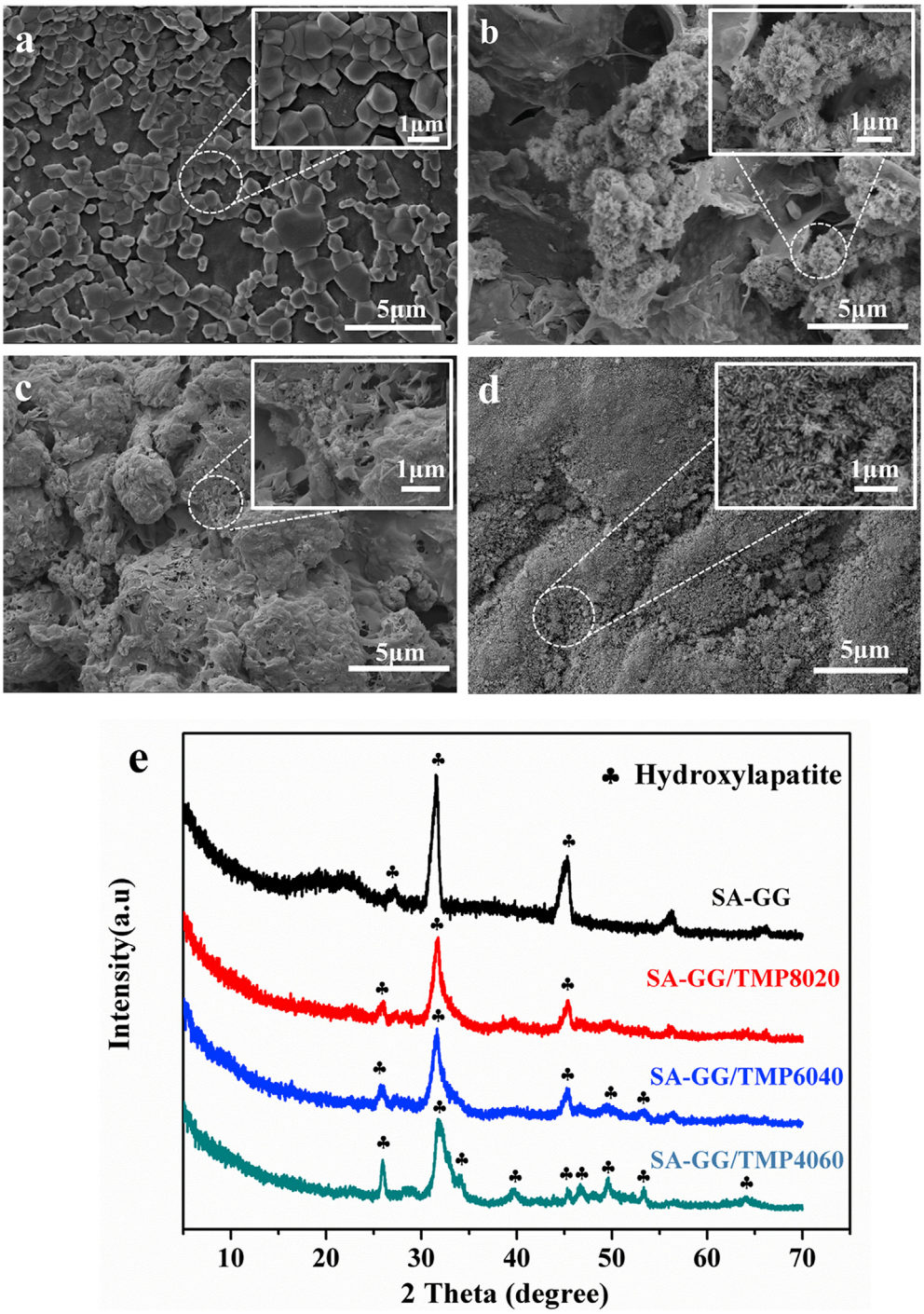

Fig. 5. The surface morphologies of (a) SA-GG, (b) SA-GG/TMP8020, (c) SA-GG/TMP6040 and (d) SA-GG/TMP4060 after immersed in SBF for 15 d. (e) The XRD patterns of mineralized samples.

when the content of TMP-BG was more than 60% (v/v), which indicated that more than 40% (v/v) of TMP-BG in the hybrid hydrogel scaffolds might not be conducive to cell growth. It is speculated that the parameters, i.e. the stiffness, released inorganic ions and surface characteristics of the SA-GG/TMP scaffold with more than 60% of inorganic TMP-BG, were not suitable for the growth of cells.

3.6. Osteogenic gene expressions

Osteogenesis-related genes results are plotted in Fig. 7 for MG-63 cells after being cultured with SA-GG, SA-GG/TMP8020, SA-GG/TMP6040 and SA-GG/TMP4060 hybrid hydrogel scaffolds for 7 d. These include collagen type I (Col-I), runt-related transcription factor 2 (RunX2), alkaline phosphatase (ALP), osteopontin (OPN), and osteocalcin (OCN). Col-I is an essential component of the extracellular matrix of bone tissue and expresses in the middle phase of osteogenesis [54], RunX2 is a specific transcription factor in early bone formation [55]. The expression levels of Col-I and RunX2 reached a peak at 5 d of culture. The upregulation of Col-I and RunX2 by the hybrid hydrogel scaffolds was more significant compared with those of SA-GG. Col-I showed an enhanced upward trend with the increase of TMP-BG (Fig. 7a and b). ALP is a marker of the middle phase of osteogenic differentiation during bone

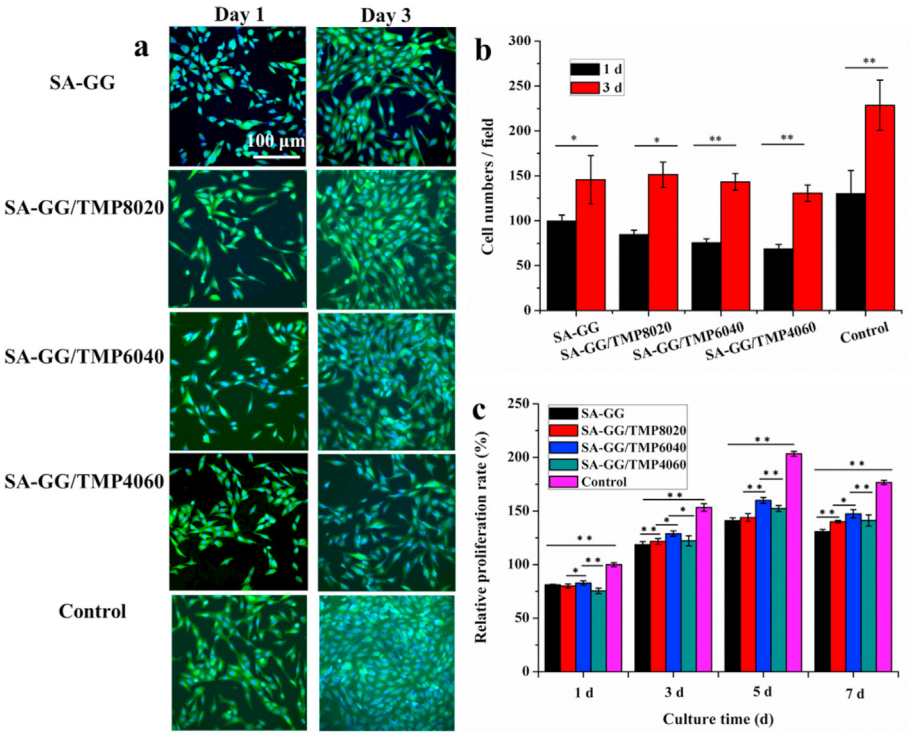

Fig. 6. (a) The fluorescence staining images of four hybrid hydrogel scaffolds after being cultured with MG-63 cells for 1 d and 3 d; (b) The average MG-63 cell numbers were calculated by Image-J software; (c) Results of the relative proliferation percent of MG-63 cells when grew on samples for 7 d. $*p < 0.05$, $**p < 0.01$; n = 3.

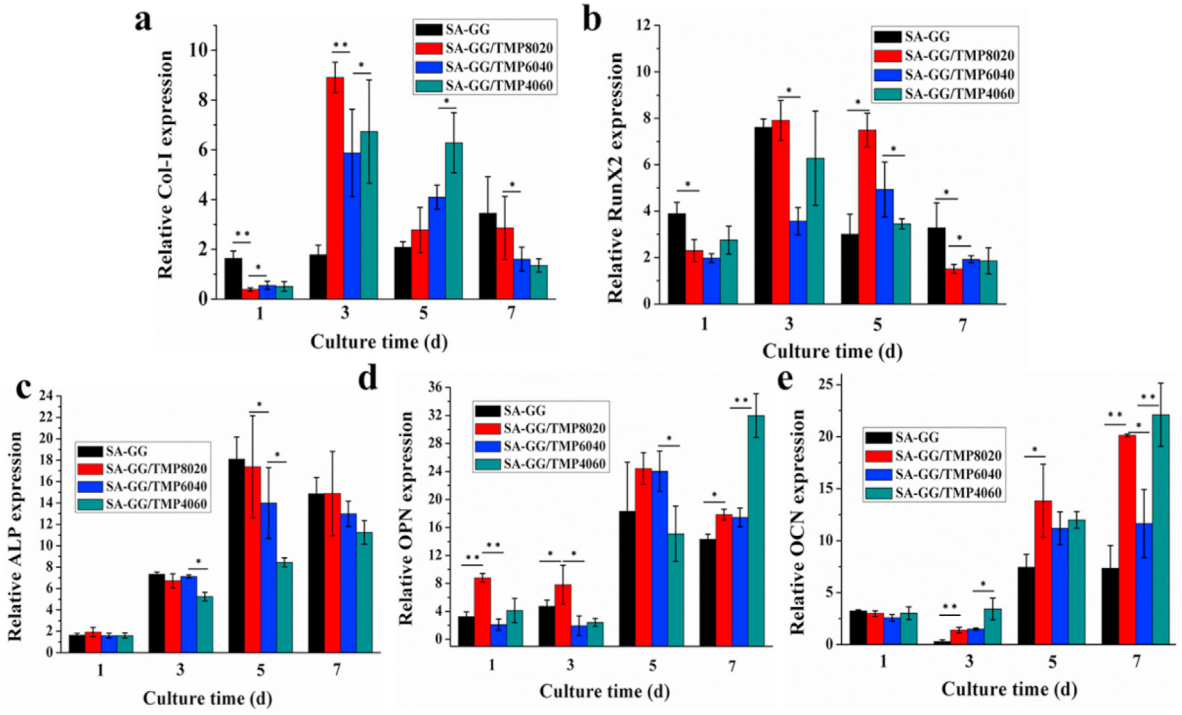

Fig. 7. The effect of hybrid hydrogel scaffolds with different ratios on quantitative expression of osteoblast-related gene mRNA in MG-63 cells. (a) Col-I; (b) RunX2; (c) ALP; (d) OPN; (e) OCN. Cell culture plate served as a control and was set as 1. $*p < 0.05$, $**p < 0.01$; n = 5.

formation accompanied by the synthesis of extracellular matrix. Over the culture time, the expression of ALP was upregulated in four groups and then stabilized at 7 d, and there was no significant difference among the four samples (Fig. 7c). OPN and OCN are specific markers in the late stage of osteogenic differentiation during bone formation in the mineralization of the extracellular matrix stage, which improves the bone mineralization ability [55]. The expression levels of both OPN and OCN had similar upward trends in the four groups. The expression levels of OPN and OCN

further increased with the increase of culture time until 7 d. The up-regulation levels of these two genes were associated with the rise of the TMP-BG, in which SA-GG/TMP4060 possessed the highest expression levels of OCN and OPN (Fig. 7d, e), indicating the best potential for bone repairing.

Considering the results of Col-I/RunX2/ALP/OPN/OCN gene expression comprehensively, bone-related genes were upregulated in four groups. The SA-GG/TMP-BG scaffolds exhibit a better ability to upregulate genes related to bone formation in comparison to those of pure SA-GG. This is attributed to the magnesium element in the hybrid hydrogel scaffold, which can promote bone growth as an essential component of bone [20,56]. The slow releasing of Mg^{2+} the hybrid hydrogel was beneficial to long-term bone repairing from TMP-BG in the hybrid hydrogel scaffold (Fig. S4).

As a result, SA-GG/TMP6040 group was chosen for further *in vivo* osteochondral repairing experiment due to its better physicochemical properties, and results of cell experiment and osteogenic gene expression.

3.7. Regulation of materials on biological functions of BMSCs

The scratch distance of the BMSCs in the SA-GG/TMP6040 group (89.5 ± 9.0 μm) was significantly lower than those of control (332.1 ± 17.0 μm) and SA-GG group (330.0 ± 24.0 μm) after 24 h of culture (Fig. 8a, c). The Transwell assay showed that the number of migrated BMSCs were nearly 2-fold higher than other two groups (Fig. 8b, d). Interestingly, there were no statistical differences between SA-GG and group in the scratch distance and migrated cell number. These results suggest that the Mg^{2+} released from the hybrid hydrogels was the main reason for enhancing BMSCs migration. Some previous studies reported that the Mg^{2+} could promote cells migration [57]. The recruitment of BMSCs to the bone defects was conducive to promoting osteochondral repair [58]. The biocompatibility of the hydrogels was further assessed by BMSC culture. Fig. 9a shows that, the results of Live/Dead assay showed that the number of live cell (green) of all samples increased between day 1 and day 3, and there were negligible dead cells (red) in the SA-GG and SA-GG/TMP6040 groups. Furthermore, there was no obvious difference on the cell density of BMSCs grew on the surface of hydrogel on day 3. A normal F-actin spreading of BMSCs was observed in all groups (Fig. 9b). These results indicated that the hydrogels possessed a good BMSCs compatibility.

The pluripotentiality of BMSCs was determined by osteogenic and chondrogenic differentiation assays. After of culture with the samples for 7 d, ALP activity and calcium nodules appeared in all groups. Compared with the control and SA-GG group , BMSCs showed enhanced ALP (Fig. 9d) and Alizarin red (Fig. 9e) staining in the SA-GG/TMP6040 groups, suggesting that the inorganic components of Mg^{2+} in the hybrid hydrogels promoted osteogenic differentiation. Additionally, the formation of proteoglycan was confirmed by the CoL II and Alcian blue staining. After 7 d of cultured with the SA-GG/TMP6040 hydrogels, immunofluorescence for CoL II showed high intensity of red fluorescence in the SA-GG/TMP6040 group (Fig. 9c). In addition, the proteoglycan expression (blue) was viewed in cytoplasm (black arrow) of BMSCs, but

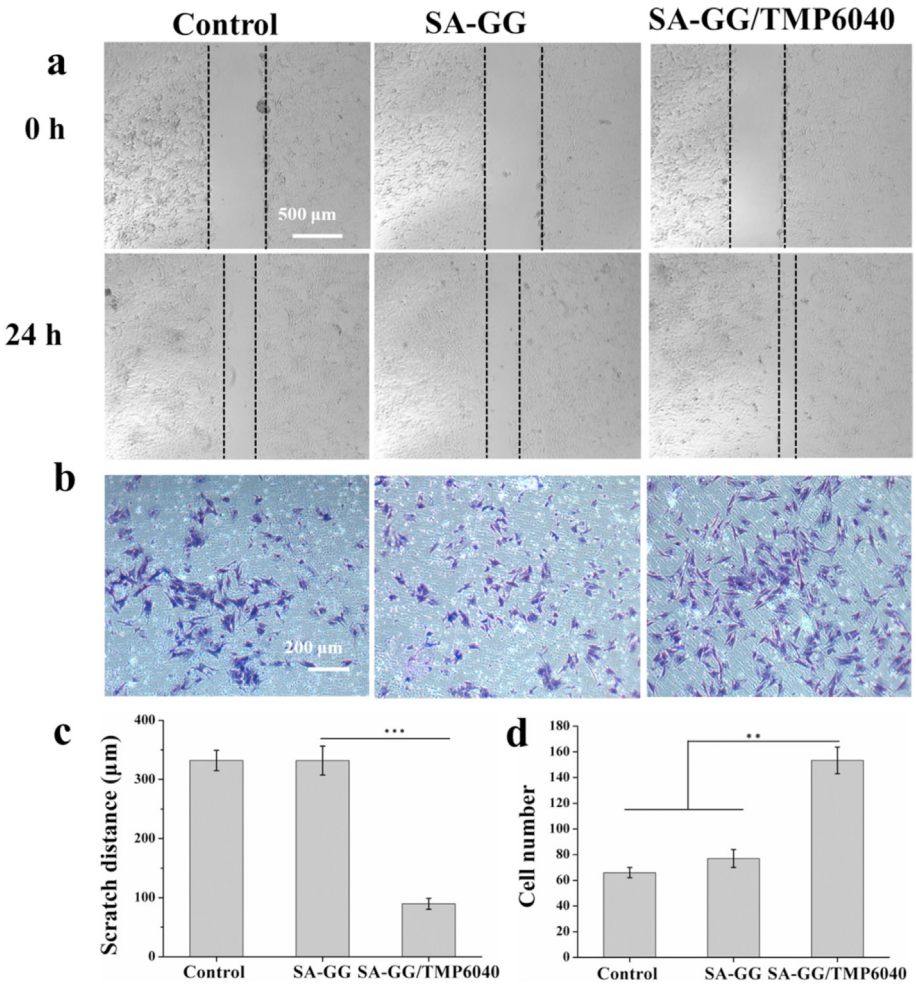

Fig. 8. Regulation of hybrid hydrogel scaffolds on biological functions of BMSCs. Migration of BMSCs analyzed using the scratch assay (a) and the Transwell assay (b). The Semi-quantitative analysis of the scratch assay (c) and the Transwell assay (d). The control group contained only culture medium. *$p < 0.05$, **$p < 0.01$; ***$p < 0.001$ n = 3.

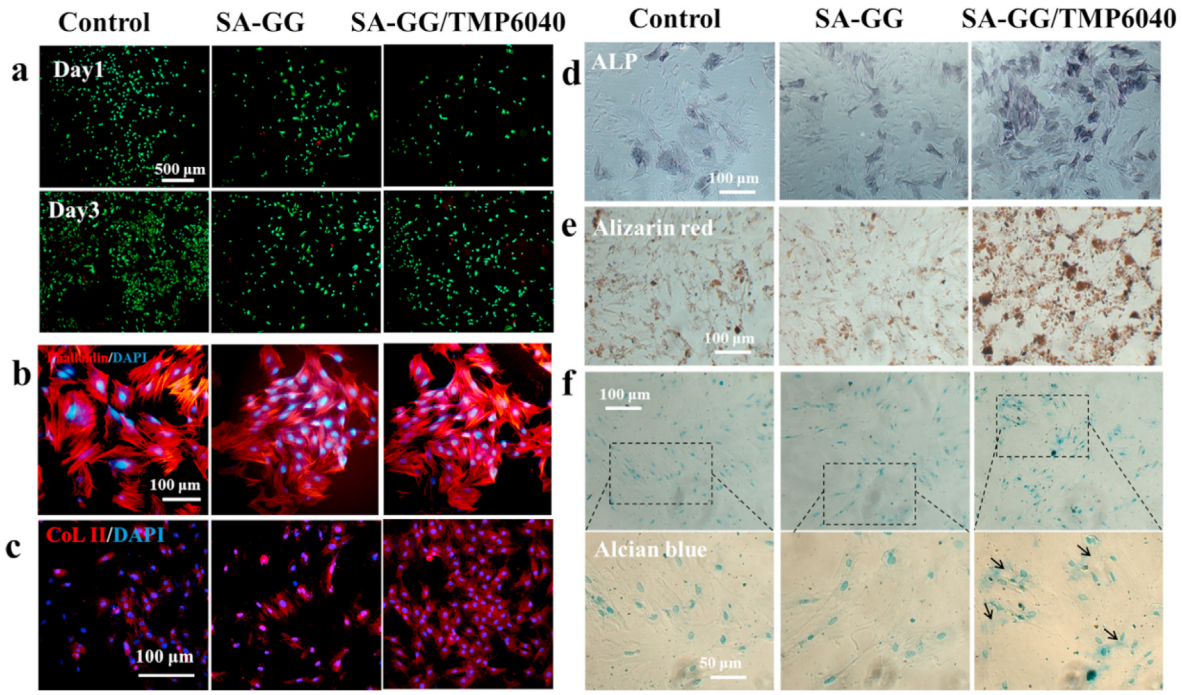

Fig. 9. Effects of hydrogels on differentiation of BMSCs. The Live/Dead staining (a) and morphology (b) of BMSCs after co-cultured with hydrogels for 3 d. Results of CoL II (c), ALP (d), Alizarin Red (e) and Alcian staining (f) of BMSCs treated with hybrid hydrogel after 7 d of culture. The control group contained only culture medium. (For interpretation of the references to colour in this figure legend, the reader is referred to the Web version of this article.)

no expression in the other two groups (Fig. 9f). The results of suggested the enhanced effect of chondrogenic differentiation in the SA-GG/TMP6040 group. In order to further observe the mature chondrocytes, a longer time is needed.

Taken together, all the above results indicate that the hybrid hydrogels can promote osteogenic and chondrogenic differentiation of BMSCs simultaneously, although the specific mechanism remains unclear. Previous study showed that, the Mg-doped hybrid scaffolds possessed positive effect on the osteogenic and chondrogenic induction [18]. The mechanism of SA-GG/TMP6040 hybrid hydrogel regulating cell function still needs further exploration.

3.8. Gross view and histological examination

Fig. S5 shows samples before and after implantation. It can be seen that, the rabbit wounds healed completely after implantation for 2 weeks. Compared with the control group, there were no significant differences in the proportion of granulocytes, lymphocytes, and intermediate cells in the implanted groups (Fig. S6), 3 d after operation. It indicated that the scaffolds did not cause a significant inflammatory reaction. The average weight of rabbits in SA-GG, SA-GG/TMP6040 and the control groups increased from 2 kg, 2.5 kg and 2.4 kg – 3 kg or so (Fig. S7) after the operation for one month, respectively. It is inferred that the scaffolds posed a negligible toxicity to animals. As shown in Fig. 10a, the osteochondral defective parts of the three groups appeared to be repaired with a certain degree after implantation for 6 weeks, but there were still clear boundaries. In particular, it was observed that there was a clear boundary between the osteochondral defect and the surrounding tissue, covered with a layer of connective tissue in the control and SA-GG groups after 12 weeks of implantation (Fig. 10b). Thus, it indicated an unsatisfactory regeneration of osteochondral defect for the control and SA-GG groups [59]. On the contrary, it was observed that the newly formed tissues had a similar smooth appearance to that of the adjacent native cartilage in the SA-GG/TMP6040 group. Specifically, regeneration of osteochondral defect was enhanced with an increase in the implantation period from 6 weeks to 12 weeks, indicating complete repair [3,59]. The ICRS macro-scoring results were shown in Fig. 10g, the ICRS scores of the SA-GG/TMP6040 group were 8 ± 1.7 and 10 ± 1, and those of the SA-GG group were 8.3 ± 0.58 and 8.7 ± 0.6 after 6 and 12 weeks of implantation, respectively, which were greater than those of the control group 6.6 ± 0.5 and 7.6 ± 0.57. According to the ICRS rating level, there was an incomplete repair when the score was 4–7, whereas it showed a better defect repair when the score was 8–11 [34]. Therefore, both the SA-GG and the SA-GG/TMP-BG6040 could promote cartilage regeneration, and the SA-GG/TMP-BG6040 group possessed the best repairing effect.

Fig. 10c–f shows the HE staining results of rabbit osteochondral defect repair 6 weeks and 12 weeks after operation. Firstly, SA-GG, SA-GG6040 groups and the control all were observed the ingrowth of new tissue (Fig. 10c) after 6 weeks of implantation. In addition, a large number of disordered cells with cartilage lacuna were observed in the SA-GG and the SA-GG/TMP6040 groups, including mainly new chondrocytes and some connective tissue (Fig. 10d), which indicated the preliminary cartilage repairing [60]. However, some cells without cartilage lacuna were disorganized in the magnified sections (black wireframe) of the control group, which inferred them to be the newly formed connective tissue. After post-implantation for 12 weeks (Fig. 10e), there was a layer of cartilage with deeply being stained and a string of chondrocytes arranged in the SA-GG/TMP6040 group. In contrast, a layer of new cartilage with disordered chondrocytes was observed in the chondral region of the control and the SA-GG groups (Fig. 10f). Fig. 10h shows the ICRS cartilage scoring result of HE. After post-implantation for 6 and 12 weeks, the ICRS scores were 11 ± 3.46 and 15.3 ± 0.58 for the SA-GG/TMP6040 group, 11.7 ± 1.2 and 12.7 ± 0.6 for the SA-GG group, and 9 ± 1 and 10.6 ± 1.5 for the control group, respectively. The ICRS scores of the SA-GG/TMP6040 groups were significantly higher than that of SA-GG and the control groups at 12 weeks of implantation although there was no significant difference among the three groups at 6 weeks. It indicated that the cartilage tissue in the SA-GG/TMP6040 group more mature than that of the other groups according to the ICRS standard [35]. In addition, there were plenty of new bone tissues in the subchondral bone region (Fig. 10c–f) of SA-GG/TMP6040 group. Fig. 10i shows the quantitative area ratio of

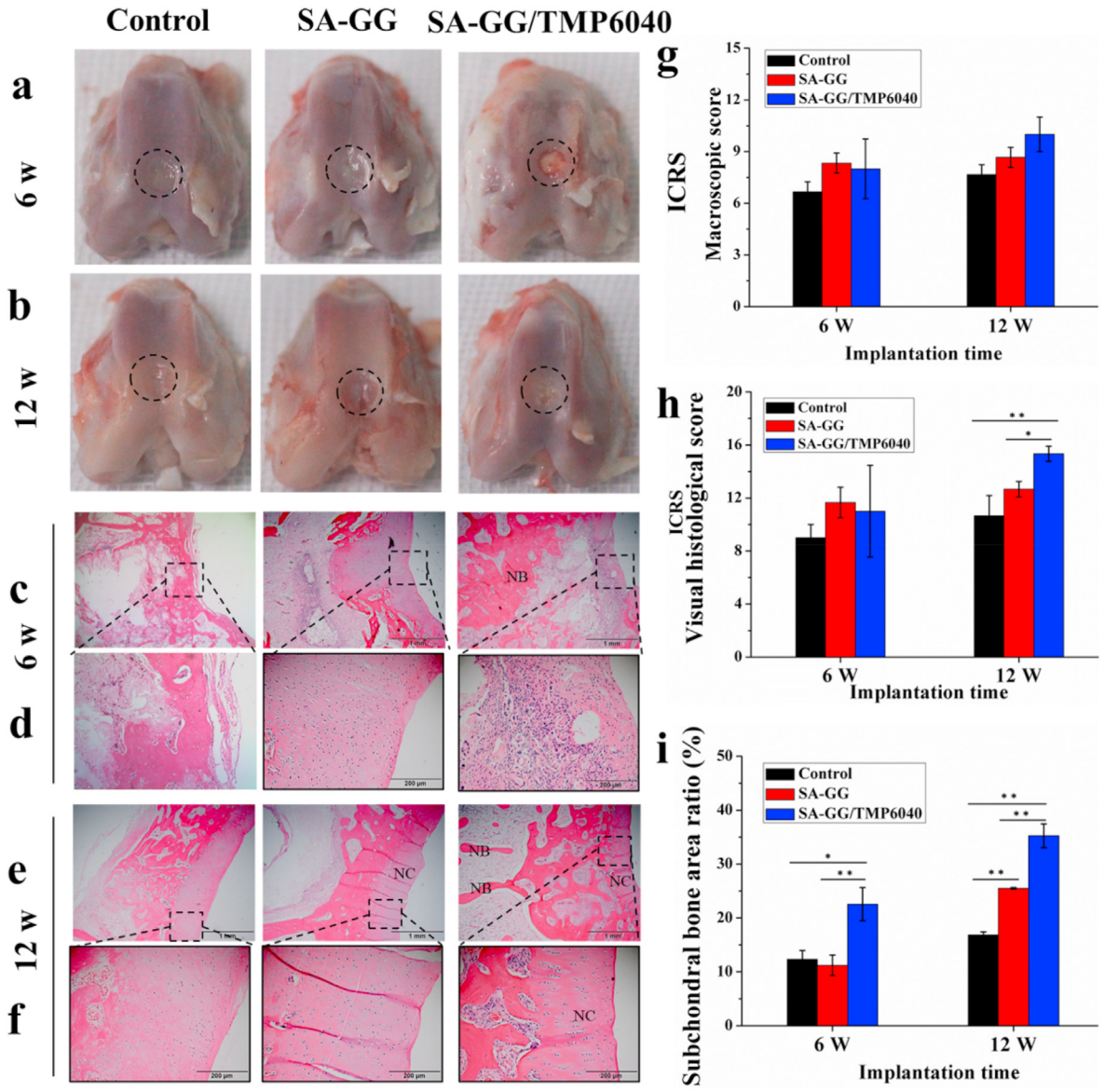

Fig. 10. The histological staining evaluation of 6 and 12 weeks of osteochondral repair. (a, b) The gross observation results after harvested specimens; (c–f) HE staining sections black wireframes indicated the repairing cartilage and subchondral bone, respectively; (g, h) ICRS scoring of cartilage repairing; (i) The areas of newly formed subchondral bone calculated from the HE images by Image-J software $*p < 0.05$, $**p < 0.01$; n = 3.

newly formed subchondral bone in three groups. The subchondral bone area ratio was 22.57% ± 3.07 and 35.27% ± 2.21 for SA-GG/TMP6040, 11.23% ± 1.91, 25.48% ± 0.15 for SA-GG group, and 12.35% ± 1.61 and 16.87% ± 0.54 for the control group after implantation for 6 and 12 weeks, respectively. The subchondral bone area ratio of SA-GG/TMP6040 group all was significantly higher than that of the control and the SA-GG groups after implantation for 6 and 12 weeks. Furthermore, the subchondral bone area ratio of SA-GG/TMP6040 group was around 2 times and 1.5 times compared to that of the control and SA-GG group at 12 weeks, respectively. Thus, the present results indicated that SA-GG/TMP6040 exhibited great potential for cartilage repair.

Results of safranine O/solid green staining images (Fig. 11) showed that the staining of the cartilage area of SA-GG/TMP6040 gradually deepened as the repair time increased by repairing time from 6 weeks (Fig. 11a and b) to 12 weeks (Fig. 11c and d). A complete tidemark appeared at 12 weeks, which is an essential sign of mature cartilage [32]. However, control and SA-GG groups still had an incomplete cartilage layer after 12 weeks of repair (Fig. 11c and d), resulting in frustrating cartilage regeneration. Results of subchondral bone regeneration show that the SA-GG/TMP6040 group had more subchondral bone formation (blue) than that of the control and SA-GG groups at 12 weeks, which was consistent with the results of HE staining. Furthermore, Fig. 11e shows that CoL II was positively stained in both scaffold groups at week 12, and the protein expressions in the SA-GG/TMP6040 were more prominent than those of SA-GG and the untreated control groups. Enlarged images of CoL II staining showed that the typical elongated chondrocytes that embedded in lacunae only viewed in the SA-GG/TMP6040 group. These results suggested that enhanced cartilage subchondral bone regeneration was observed in the hybrid hydrogel group. Studies have demonstrated that Mg^{2+} can promote bone defect regeneration [16], but its mechanism is unclear.

For the regeneration of subchondral bone, most researchers believe that Mg^{2+} can stimulate periosteal nerve endings to upregulate the expression of calcitonin gene-related peptide (cGRP), thereby promoting bone formation [61]. Mg^{2+} as the bioactive elements has been widely used to enhance the attachment and differentiation of osteoblastic cells, as well as accelerating vascularization and mineralization to enhance bone regeneration [62]. Additionally, Mg^{2+} can promote the polarization

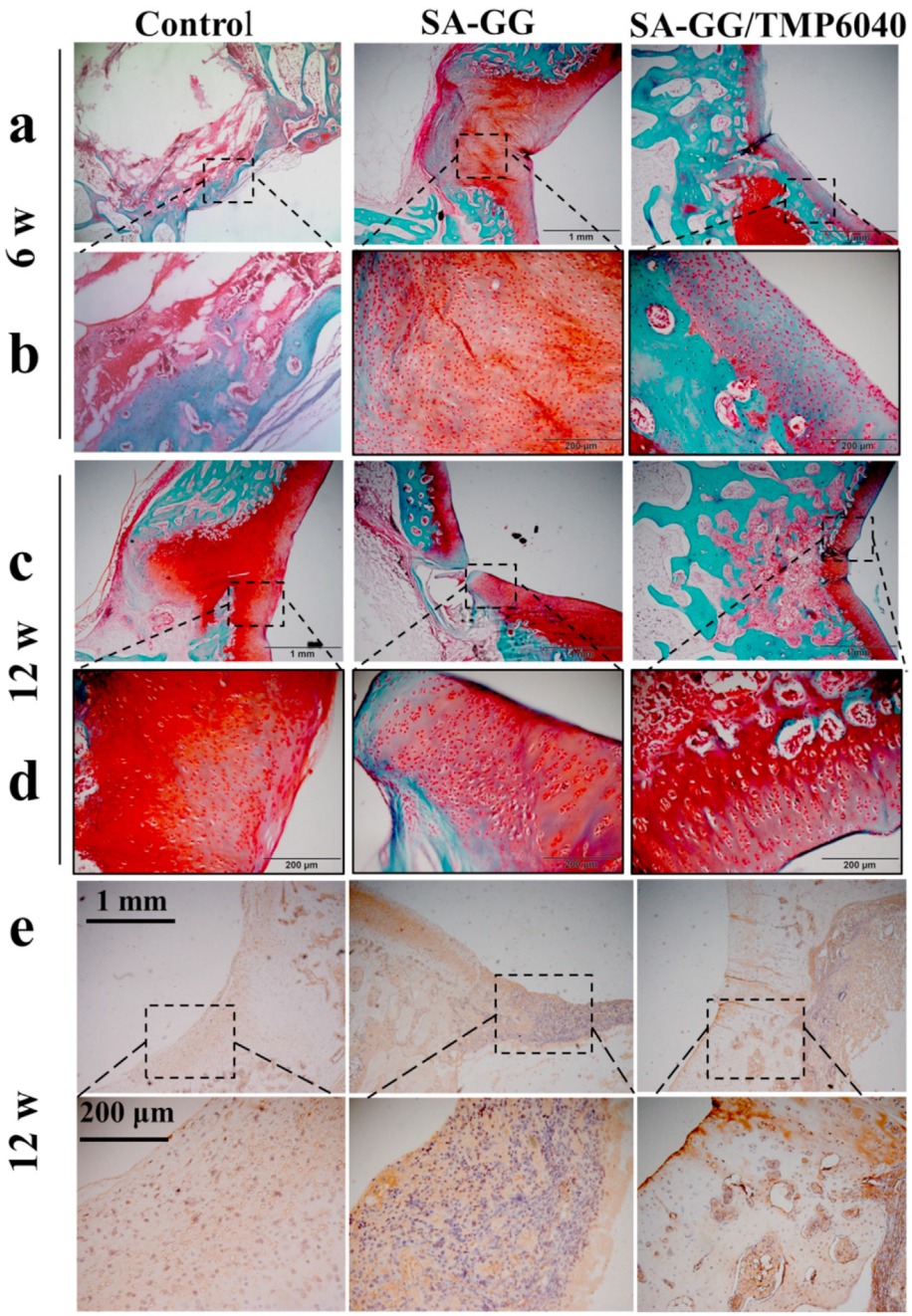

Fig. 11. Results of safranin-O/solid green staining after 6 weeks (a, b) and 12 weeks (c, d) bone/cartilage repair. Regions with red and blue indicate the newly formed cartilage and bone, respectively. (e) Immunohistochemical staining of collagen II at the 12 weeks. Black wireframe shows the cartilage layer. (For interpretation of the references to colour in this figure legend, the reader is referred to the Web version of this article.)

of macrophages from M1 to M2 phenotype and reduce the inflammation in the repair area, which is another important mechanism to promote bone repair [63]. Therefore, for the SA-GG/TMP6040 group, the slowly released Mg^{2+} from the TMP-BG was positive to accelerate the regeneration of subchondral bone (Fig. S4). In addition, the Ca^{2+} used in crosslinked hydrogel network might have a positive impact on osteoblasts and bone formation. The dynamic changes in Ca^{2+} concentrations in the bone microenvironments could directly accelerate the mineralization process of new bone and effectively modulate MSCs phenotype and thereby contribute to bone regeneration [64].

For cartilage regeneration, Mg^{2+} can not only directly promote the proliferation of chondrocytes, but also indirectly promote the chondrogenesis of human synovial mesenchymal stem cells by inhibiting the production of inflammatory cytokines and using integrins [65,66]. In addition, there was closely cross talk between articular cartilage and subchondral bone [67]. Previous studies *in vivo* suggested that articular cartilage nutrition was mediated by subchondral bone [68]. In addition, the biomechanical characteristics and the chemokines, cytokines and proteases of subchondral bone were conducive to promoting chondrocyte activation to promote cartilage regeneration [67]. We speculate that the implantation of a hybrid SA-GG/TMP6040 scaffold firstly promoted the restoration of subchondral bone, and then induced the regeneration of the cartilage layer. Therefore, the SA-GG/TMP6040 group exhibited higher osteogenic activity than SA-GG and the control groups did. However, the specific mechanism still needs further studies in our next work.

3.9. Fluorescent bone labeling

Various fluorescent dyes can combine with the newly formed bone and subchondral bone to observe the dynamic regeneration process of bone at different times, which will not affect the mineralization of new bones [16,69]. As shown in Fig. 12, the dynamic regeneration of subchondral bone was revealed by the new mineralization bone matrix marked with different colors by calcein (green), tetracycline (blue) and alizarin red (red) after implantation for 12 weeks, respectively. The results of confocal microscopy showed the mineralization of the new bone matrix during the dynamic regeneration process. The overlay bone fluorescence labeling results showed that the newly formed subchondral bone was significantly higher in the SA-GG/TMP6040 than that of the control and the SA-GG groups (Fig. 12a). Calcein labeled bone matrix formation possessed the highest green fluorescence intensity (from 6 to 8 weeks, Fig. 12b), followed by tetracycline with blue fluorescence (from 8 to 10 weeks, Fig. 12c) and alizarin red with red fluorescence (from 10 to 12 weeks, Fig. 12d). In particular, the SA-GG/TMP6040 group exhibited a more intense and extensive fluorescence signal than that of the control and the SA-GG groups. In addition, quantitative overlay fluorescence intensities were 38.2%, 26.1% and 17.9% for the SA-GG/TMP6040, the SA-GG and control groups, respectively, and the first one was significantly higher than that of the control and SA-GG groups (Fig. 12e). Separately, the fluorescence intensity of calcein was significantly higher in the SA-GG/TMP6040 group (11.3%) than in the control group (5.5%) and the SA-GG group (5.3%) (Fig. 12f). Also, the significantly higher intensities of tetracycline and alizarin red were observed in the SA-GG/TMP6040 group (19.4% and 16.7%, respectively) related to the control (9.2% and 12.6%, respectively) and the SA-GG groups (14.1% and 14.5%, respectively) (Fig. 12g and h). The highest tetracycline fluorescence intensity was observed in SA-GG/TMP6040 group, suggesting a rapid new bone matrix mineralization process during the first 8 weeks of implantation. Between 10 and 12 weeks, the reduction or the similarity of the fluorescence intensity of the SA-GG/TMP6040 and the SA-GG groups was mainly attributed to the period of bone mature [69]. It could be found that the subchondral bone in all groups was slowly repaired and matured after implantation from 6 to 12 weeks, but the highest new subchondral bone formation appeared in the SA-GG/TMP6040 group. It indicated that the SA-GG/TMP6040 had the best performance to promote the repairing of subchondral bone. Combining with results of HE, safranin-O and solid green staining, it confirmed that the SA-GG/TMP6040 could successfully promote the integration repairing of osteochondral defects. However, there is still a challenge for improvement in the repairing rate of the bone defect of the SA-GG/TMP6040 scaffolds at 12 weeks. In the future, we will print the SA-GG/TMP-BG6040 hybrid bioink into porous scaffolds loaded with cells or bioactive factors, e.g. TGF-β or BMPs *via* a 3D printing technique to further improve their osteochondral repairing rate.

4. Conclusion

This study developed a novel hybrid hydrogel composed of organic SA-GG and thixotropic inorganic TMP-BG to enhance its osteochondral repair. SA-GG/TMP-BG hybrid hydrogels presented the controllable mechanical, injectability, rheology properties and porosities, as well as superior osteogenic activity to meet the repairing of subchondral bone and cartilage. Compared with pure SA-GG hydrogels, the hybrid hydrogel scaffolds promoted the attachment, viability and proliferation of MG-63 cells *in vitro*. Additionally, the up-regulation of an osteogenic related gene was found in the hybrid groups. The SA-GG/TMP6040 hybrid hydrogel promoted BMSCs migration, adhesion, osteogenic and chondrogenic differentiation. *In vivo* animal evaluation further verified that the hybrid

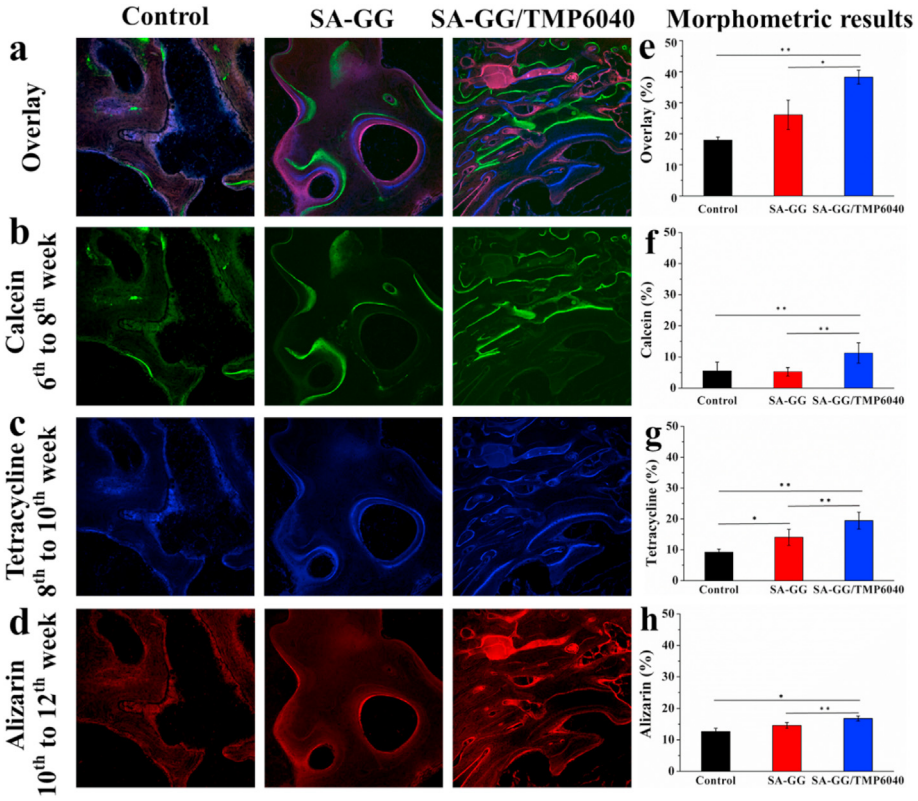

Fig. 12. Fluorescent bone labeling results of the regeneration subchondral bone after 12 weeks of implantation. (a) The overlay images of three fluorescent formation markers; (b) calcein, (c) tetracycline, (d) alizarin; and (e–h) the quantitative results of their fluorescence densities. $^{*}p < 0.05$, $^{**}p < 0.01$; n = 3.

hydrogel scaffolds could successfully firstly induce subchondral bone repairing, and then promote the cartilage reconstruction. The inorganic TMP-BG endowed the excellent osteogenic activity of SA-GG/TMP, which plays a key role in successful osteochondral repairing. Although a long term *in vivo* study is needed, the current work confirmed that the SA-GG/TMP-BG hybrid scaffolds are suitable for osteochondral regeneration and might have great potential in other tissue repairs. Excellent injectability and bioactivity of the hybrid hydrogels are expected to enable potential applications in 3D bioprinting and minimally invasive surgery.

Author contributions

You Chen., Yuanyuan Chen and Xiong Xiong. performed the experiments, analyzed the data, created the figures, and wrote the manuscript. Rongwei Cui contributed to compression test and performed the swelling test. Chen Wang. assited with editing the manuscript. Guowei Zhang helped perform the cell experiments, and Jie Weng., assited with writing and editing the manuscript. Shuxin Qu., and Dongqin Xiao., conceived the project, designed the experiments and provided funding.

Declaration of competing interest

The authors declare that they have no known competing financial interests or personal relationships that could have appeared to influence the work reported in this paper.

Acknowledgements

This study is partly supported by the following programs: National Natural Science Foundation of China (Grant No. 52035012), Basic Research Foundation Key Project of Sichuan Province (2021JY0046), Fundamental Research Funds for the Central Universities (2682020ZT91).

Appendix A. Supplementary data

Supplementary data to this article can be found online at https://doi.org/10.1016/j.mtbio.2022.100261.

References

[1] L.B. Zhou, G. Van Osch, J. Malda, M.J. Stoddart, Y.X. Lai, R.G. Richards, et al., Innovative tissue-engineered strategies for osteochondral defect repair and regeneration: current progress and challenges, Adv. Healthc. Mater. 9 (2020).
[2] D.J.H.J.C. Huey, K.A. Athanasiou, Unlike bone, cartilage regeneration remains elusive, Science 338 (2012) 917–921.
[3] W.E.E.K.S. Wei, H. Dai, Articular cartilage and osteochondral tissue engineering techniques: recent advances and challenges, Bioact. Mater. 6 (2021) 4830–4855.
[4] A. Saxena, L. Shou, A novel technique to treat hallux rigidus in athletic patients with central osteochondral defects: preliminary report on 12 cases, J. Foot Ankle Surg. 60 (2021) 845–849.
[5] C. Delman, C. White, K. Natsuhara, C. Kreulen, E. Giza, Treatment of osteochondral lesions of the talus with matrix-induced autologous chondrocyte implantation (MACI), Tech. Foot Ankle Surg. 19 (2020) 184–189.
[6] L. Xin, C. Zhang, W.-X. Xu, F.-H. Zhong, Fan S-Weeks, Z.-B. Wang, Current advances on surgical treatment for knee articular cartilage injuries, Zhongguo Shang = China J. Orthopaed. Traumatol. 31 (2018) 281–285.
[7] E.A. Makris, A.H. Gomoll, K.N. Malizos, J.C. Hu, K.A. Athanasiou, Repair and tissue engineering techniques for articular cartilage, Nat. Rev. Rheumatol. 11 (2015) 21–34.
[8] X. Hu, Y. Wang, Y. Tan, J. Wang, H. Liu, Y. Wang, et al., A difunctional regeneration scaffold for knee repair based on aptamer-directed cell recruitment, Adv. Mater. 29 (2017).
[9] Y. Zhang, X. Liu, L. Zeng, J. Zhang, J. Zuo, J. Zou, et al., Polymer fiber scaffolds for bone and cartilage tissue engineering, Adv. Funct. Mater. (2019) 1903279.
[10] L. Bi, D. Li, J. Liu, Y.Y. Hu, P. Yang, B. Yang, et al., Fabrication and characterization of a biphasic scaffold for osteochondral tissue engineering, Mater. Lett. 65 (2011) 2079–2082.
[11] H. Zhang, H.F. Huang, G.R. Hao, Y.S. Zhang, H. Ding, Z.J. Fan, et al., 3D printing hydrogel scaffolds with nanohydroxyapatite gradient to effectively repair osteochondral defects in rats, Adv. Funct. Mater. (2021) 31.
[12] J. Yang, Y.S. Zhang, K. Yue, A. Khademhosseini, Cell-laden hydrogels for osteochondral and cartilage tissue engineering, Acta Biomater. 57 (2017) 1–25.
[13] W.E.E.K.S. Wei, Y.Z. Ma, X.D. Yao, W.Y. Zhou, X.Z. Wang, C.L. Li, et al., Advanced hydrogels for the repair of cartilage defects and regeneration, Bioact. Mater. 6 (2021) 998–1011.
[14] M.P. Lutolf, J.A. Hubbell, Synthetic biomaterials as instructive extracellular microenvironments for morphogenesis in tissue engineering, Nat. Biotechnol. 23 (2005) 47–55.
[15] Y. Du, H. Liu, Q. Yang, S. Wang, J. Wang, J. Ma, et al., Selective laser sintering scaffold with hierarchical architecture and gradient composition for osteochondral repair in rabbits, Biomaterials 137 (2017) 37–48.
[16] Y. Lai, Y. Li, H. Cao, J. Long, X. Wang, L. Li, et al., Osteogenic magnesium incorporated into PLGA/TCP porous scaffold by 3D printing for repairing challenging bone defect, Biomaterials 197 (2019) 207–219.
[17] D.J. Munoz-Pinto, R.E. McMahon, M.A. Kanzelberger, A.C. Jimenez-Vergara, M.A. Grunlan, M.S. Hahn, Inorganic-organic hybrid scaffolds for osteochondral regeneration, J. Biomed. Mater. Res. 94 (2010) 112–121.
[18] X.N. Yu, T.F. Zhao, Y.Y. Qi, J.Y. Luo, J.H. Fang, X.Y. Yang, et al., In vitro chondrocyte responses in Mg-doped wollastonite/hydrogel composite scaffolds for osteochondral interface regeneration, Sci. Rep. 8 (2018) 9.
[19] E. Kon, M. Delcogliano, G. Filardo, M. Fini, G. Giavaresi, S. Francioli, et al., Orderly osteochondral regeneration in a sheep model using a novel nano-composite multilayered biomaterial, J. Orthop. Res. 28 (2010) 116–124.
[20] M. Laurenti, A. Al Subaie, M.N. Abdallah, A.R.G. Cortes, J.L. Ackerman, H. Vali, et al., Two-dimensional magnesium phosphate nanosheets form highly thixotropic gels that up-regulate bone formation, Nano Lett. 16 (2016) 4779–4787.
[21] W.H. Wang, J. Shen, Y. Meng, M.M. Ye, S.Z. Lin, Q. Zhao, et al., Magnesium cationic cue enriched interfacial tissue microenvironment nurtures the osseointegration of gamma-irradiated allograft bone, Bioact. Mater. 10 (2022) 32–47.
[22] N. Ostrowski, A. Roy, P.N. Kumta, Magnesium phosphate cement systems for hard tissue applications: a revie weeks, ACS Biomater. Sci. Eng. 2 (2016) 1067–1083.
[23] J.K. Xu, P.J. Hu, X.T. Zhang, J.J. Chen, J.L. Wang, J.T. Zhang, et al., Magnesium implantation or supplementation ameliorates bone disorder in CFTR-mutant mice through an ATF4-dependent Wnt/beta-catenin signaling, Bioact. Mater. 8 (2022) 95–108.
[24] G. Mestres, M.-P. Ginebra, Novel magnesium phosphate cements with high early strength and antibacterial properties, Acta Biomater. 7 (2011) 1853–1861.
[25] Y. Wu, Y.M. Wang, Zhao Dweeks, N. Zhang, H. Li, J. Li, et al., In vivo study of microarc oxidation coated Mg alloy as a substitute for bone defect repairing: degradation behavior, mechanical properties, and bone response, Colloids Surf. B Biointerfaces 181 (2019) 349–359.
[26] Y. Chen, Y. Wang, Q. Yang, Y. Liao, B. Zhu, G. Zhao, et al., A novel thixotropic magnesium phosphate-based bioink with excellent printability for application in 3D printing, J. Mater. Chem. B 6 (2018) 4502–4513.
[27] Y. Chen, X. Xiong, X. Liu, R. Cui, C. Wang, G. Zhao, et al., 3D bioprinting of shear-thinning hybrid bioink with excellent bioactivity derived from gellan/alginate and thixotropic magnesium phosphate-based gel, J. Mater. Chem. B 8 (2020) 5500–5514.
[28] S. Wüst, M.E. Godla, R. Müller, S. Hofmann, Tunable hydrogel composite with two-step processing in combination with innovative hardware upgrade for cell-based three-dimensional bioprinting, Acta Biomater. 10 (2014) 630–640.
[29] T. Kokubo, H. Takadama, How useful is SBF in predicting in vivo bone bioactivity? Biomaterials 27 (2006) 2907–2915.
[30] Y. Liu, F. Shi, L. Bo, Zhi Weeks, J. Weng, S. Qu, A novel alginate-encapsulated system to study biological response to critical-sized wear particles of UHMWPE loaded with alendronate sodium, Mater. Sci. Eng. C, Mater. Biol. Appl. 79 (2017) 679–686.
[31] Q. Liu, X.X. Zhang, Y. Jiao, X. Liu, Y.R. Wang, S.L. Li, et al., In vitro cell behaviors of bone mesenchymal stem cells derived from normal and postmenopausal osteoporotic rats, Int. J. Mol. Med. 41 (2018) 669–678.
[32] L. Han, J. Xu, X. Lu, D. Gan, Z. Wang, K. Wang, et al., Biohybrid methacrylated gelatin/polyacrylamide hydrogels for cartilage repair, J. Mater. Chem. B 5 (2017) 731–741.
[33] M.P. van den Borne, N.J. Raijmakers, J. Vanlauwe, J. Victor, S.N. de Jong, J. Bellemans, et al., International cartilage repair society (ICRS) and oswestry macroscopic cartilage evaluation scores validated for use in autologous chondrocyte implantation (ACI) and microfracture, Osteoarthritis Cartilage 15 (2007) 1397–1402.
[34] R.U. Kleemann, D. Krocker, A. Cedraro, J. Tuischer, G.N. Duda, Altered cartilage mechanics and histology in knee osteoarthritis: relation to clinical assessment (ICRS Grade), Osteoarthritis Cartilage 13 (2005) 958–963.
[35] P. Mainil-Varlet, T. Aigner, M. Brittberg, P. Bullough, A. Hollander, E. Hunziker, R. Kandel, S. Nehrers, K. Pritzker, S. Roberts, E. Stauffer, Histological assessment of cartilage repair: a report by the histology endpoint committee of the international cartilage repair society (ICRS), J. Bone Joint Surg. 85 (2003) 45–57.
[36] B. Von Lospichl, S. Hemmati-Sadeghi, P. Dey, T. Dehne, R. Haag, M. Sittinger, et al., Injectable hydrogels for treatment of osteoarthritis - a rheological study, Colloids Surf. B Biointerfaces 159 (2017) 477–483.
[37] T. Pénzes, I. Csóka, I. Erős, Rheological analysis of the structural properties effecting the percutaneous absorption and stability in pharmaceutical organogels, Rheol. Acta 43 (2004) 457–463.
[38] K. Markstedt, A. Mantas, I. Tournier, H.M. Avila, D. Hagg, P. Gatenholm, 3D bioprinting human chondrocytes with nanocellulose-alginate bioink for cartilage tissue engineering applications, Biomacromolecules 16 (2015) 1489–1496.

[39] A.C. Daly, S.E. Critchley, E.M. Rencsok, D.J. Kelly, A comparison of different bioinks for 3D bioprinting of fibrocartilage and hyaline cartilage, Biofabrication 8 (2016), 045002.
[40] K. Yue, G. Trujillo-de Santiago, M.M. Alvarez, A. Tamayol, N. Annabi, A. Khademhosseini, Synthesis, properties, and biomedical applications of gelatin methacryloyl (GelMA) hydrogels, Biomaterials 73 (2015) 254–271.
[41] J. Ran, P. Jiang, S. Liu, G. Sun, P. Yan, X. Shen, et al., Constructing multi-component organic/inorganic composite bacterial cellulose-gelatin/hydroxyapatite double-network scaffold platform for stem cell-mediated bone tissue engineering, Mater. Sci. Eng. C, Mater. Biol. Appl. 78 (2017) 130–140.
[42] A.K. Panda, B. Basu, Functionalized fluoropolymer-compatibilized elastomeric bilayer composites for osteochondral repair: unraveling the role of substrate stiffness and functionalities, ACS Appl. Bio Mater. 4 (2021) 8543–8558.
[43] A.R. Gannon, T. Nagel, A.P. Bell, N.C. Avery, D.J. Kelly, Postnatal changes to the mechanical properties of articular cartilage are driven by the evolution of its collagen network, Eur. Cell. Mater. 29 (2015) 105–123.
[44] H.N. Chia, M.L. Hull, Compressive moduli of the human medial meniscus in the axial and radial directions at equilibrium and at a physiological strain rate, J. Orthop. Res. 26 (2008) 951–956.
[45] P. Bursac, S. Arnoczky, A. York, Dynamic compressive behavior of human meniscus correlates with its extra-cellular matrix composition, Biorheology 46 (2009) 227–237.
[46] S. Jana, A. Das, A.K. Nayak, K.K. Sen, S.K. Basu, Aceclofenac-loaded unsaturated esterified alginate/gellan gum microspheres: in vitro and in vivo assessment, Int. J. Biol. Macromol. 57 (2013) 129–137.
[47] E. Karamian, M. Abdellahi, H. Gheisari, Fluorine-substituted HA reinforced with zircon as a novel nano-biocomposite ceramic: preparation and characterization, Int. J. Mater. Res. 106 (2015) 1285–1290.
[48] S.K.S.K. Balavandy, Z.Z. Abidin, Rapid and green synthesis of silver nanoparticles via sodium alginate media, Int. J. Electrochem. Sci. 10 (2015) 486–497.
[49] P. Vashisth, K. Nikhil, P. Roy, P.A. Pruthi, R.P. Singh, V. Pruthi, A novel gellan-PVA nanofibrous scaffold for skin tissue regeneration: fabrication and characterization, Carbohydr. Polym. 136 (2016) 851–859.
[50] T.S. Pathak, J.S. Kim, S.-J. Lee, D.-J. Baek, K.-J. Paeng, Preparation of alginic acid and metal alginate from algae and their comparative study, J. Polym. Environ. 16 (2008) 198–204.
[51] N. Zanjanizadeh Ezazi, M.A. Shahbazi, Y.V. Shatalin, E. Nadal, E. Makila, J. Salonen, et al., Conductive vancomycin-loaded mesoporous silica polypyrrole-based scaffolds for bone regeneration, Int. J. Pharm. 536 (2018) 241–250.
[52] J HS, Porous scaffold design for tissue engineering, Nat. Mater. 4 (2005) 518–524.
[53] Wake M C PCWEEKS, A.G. Mikos, Pore morphology effects on the fibrovascular tissue growth in porous polymer substrates, Cell Transplant. 3 (1994) 339–343.
[54] R.T. Franceschi, G. Xiao, D. Jiang, R. Gopalakrishnan, S. Yang, E. Reith, Multiple signaling pathways converge on the cbfa1/runx2 transcription factor to regulate osteoblast differentiation, Connect. Tissue Res. 44 (2009) 109–116.
[55] W.E.E.K.S. Tang, G.M. Policastro, G. Hua, K. Guo, J. Zhou, C. Wesdemiotis, et al., Bioactive surface modification of metal oxides via catechol-bearing modular peptides: multivalent-binding, surface retention, and peptide bioactivity, J. Am. Chem. Soc. 136 (2014) 16357–16367.
[56] G. Mestres, M.P. Ginebra, Novel magnesium phosphate cements with high early strength and antibacterial properties, Acta Biomater. 7 (2011) 1853–1861.
[57] S.L. Zhu, Q.Y. Dai, L.T. Yao, Z.T. Wang, Z.C. He, M.C. Li, et al., Engineered multifunctional nanocomposite hydrogel dressing to promote vascularization and anti-inflammation by sustained releasing of Mg2+ for diabetic wounds, Compos. B Eng. 231 (2022) 16.
[58] F.X. Zhang, P. Liu, W.E.E.K.S. Ding, Q.B. Meng, D.H. Su, Q.C. Zhang, et al., Injectable Mussel-Inspired highly adhesive hydrogel with exosomes for endogenous cell recruitment and cartilage defect regeneration, Biomaterials 278 (2021) 121169.
[59] J.Q. Chen, J.B. Yang, L. Wang, Zhang Xweeks, B.C. Heng, D.A. Wang, et al., Modified hyaluronic acid hydrogels with chemical groups that facilitate adhesion to host tissues enhance cartilage regeneration, Bioact. Mater. 6 (2021) 1689–1698.
[60] Y. Han, B. Jia, M.F. Lian, B.B. Sun, Q. Wu, B.L. Sun, et al., High-precision, gelatin-based, hybrid, bilayer scaffolds using melt electro-writing to repair cartilage injury, Bioact. Mater. 6 (2021) 2173–2186.
[61] Y. Zhang, J. Xu, Y.C. Ruan, M.K. Yu, M. O'Laughlin, H. Wise, et al., Implant-derived magnesium induces local neuronal production of CGRP to improve bone-fracture healing in rats, Nat. Med. 22 (2016) 1160–1169.
[62] Z.Y. Yuan, P.F. Wei, Y.Q. Huang, W.X. Zhang, F.Y. Chen, X. Zhang, et al., Injectable PLGA microspheres with tunable magnesium ion release for promoting bone regeneration, Acta Biomater. 85 (2019) 294–309.
[63] X.R. Qiao, J. Yang, Y.L. Shang, S. Deng, D.S.Y. Yao, Z. Wang, et al., Magnesium-doped nanostructured titanium surface modulates macrophage-mediated inflammatory response for ameliorative osseointegration, Int. J. Nanomed. 15 (2020) 7185–7198.
[64] M.N. Lee, H.S. Hwang, S.H. Oh, A. Roshanzadeh, Kim Jweeks, J.H. Song, et al., Elevated extracellular calcium ions promote proliferation and migration of mesenchymal stem cells via increasing osteopontin expression, Exp. Mol. Med. 50 (2018) 16.
[65] T. Hu, H.T. Xu, C.Y. Wang, H. Qin, Z.Q. An, Magnesium enhances the chondrogenic differentiation of mesenchymal stem cells by inhibiting activated macrophage-induced inflammation, Sci. Rep. 8 (2018) 13.
[66] M. Shimaya, T. Muneta, S. Ichinose, K. Tsuji, I. Sekiya, Magnesium enhances adherence and cartilage formation of synovial mesenchymal stem cells through integrins, Osteoarthritis Cartilage 18 (2010) 1300–1309.
[67] A.R. Sharma, S. Jagga, S.S. Lee, J.S. Nam, Interplay between cartilage and subchondral bone contributing to pathogenesis of osteoarthritis, Int. J. Mol. Sci. 14 (2013) 19805–19830.
[68] T. Malinin Eao, Articular cartilage nutrition is mediated by subchondral bone: a long-term autograft study in baboons, Osteoarthritis Cartilage 8 (2000) 483–491.
[69] R. Martins, T.M. Cestari, R.V.N. Arantes, P.S. Santos, R. Taga, M.J. Carbonari, et al., Osseointegration of zirconia and titanium implants in a rabbit tibiae model evaluated by microtomography, histomorphometry and fluorochrome labeling analyses, J. Periodontal. Res. 53 (2018) 210–221.